Many studies in HEAs are focused on the equiatomic compositions, in which the single-phase solid solution stabilizes due to the high configurational entropy [78]. However, these alloy systems are deficient in guaranteeing desired properties. For instance, Cantor HEA is well-studied alloy that has excellent ductility and high toughness even at cryogenic temperature, but its low yield strength at room temperature renders it useless for most structural applications [139]. So, researchers have been focussing on the dual-phase structure in HEAs for enhanced strengths [139]. However, with dual-phase structures, attempts were made to employ precipitation strengthened to further improve the strength of HEA systems [287]. In the present work, the non-equiatomic $Fe_{40}Mn_{20}Cr_{20-x}Ni_xTi_{10}Al_{10}$ (x = 0, 5, and 10 at. %) HEAs were prepared using mechanical alloying followed by spark plasma sintering. The alloying behaviour, microstructure, and thermal stability of the milled powder samples were done systematically. After SPS, the structure, microstructure, mechanical, wear, and biocompatibility properties were also evaluated.

6.1 Melting point prediction of the Fe-based HEAs

The predicted values of the melting point using different approaches i.e., machine learning approach, rule of mixture and ThermoCalc of the HEA1, HEA2 and HEA3 is listed in Table 6.1.

Table 6.1: Melting point of the various Fe-based HEAs with different approaches.

	HEA1	**HEA2**	**HEA3**
Machine learning (°C)	1457	1440	1416
Rule of mixture (°C)	1479	1455	1432
ThermoCalc (°C)	1390	1367	1300

The formulae used to calculate the melting point through the different approaches are given in section 2.8. The values of the possible binary liquidus temperatures in the HEA1, HEA2, and

HEA3 were given in Table 6.2. Among the above-mentioned techniques for melting point prediction, the ML approach has reached the closest to the experimental meting point in the HEAs [229].

Table 6.2: The values of liquidus temperature of all the binary alloys in the Fe-based HEAs.

Binary Alloys	Liquidus Temperature (°C)		
	HEA1	HEA2	HEA3
Fe-Mn	1400	1390	1390
Fe-Cr	1520	1538	1513
Fe-Ni	---	1500	1480
Fe-Ti	1380	1390	1390
Fe-Al	1520	1520	1520
Mn-Cr	1580	1550	1420
Mn-Ni	---	1110	1020
Mn-Ti	1325	1325	1325
Mn-Al	1080	1300	1300
Cr-Ni	---	1590	1345
Cr-Ti	1540	1560	1410
Cr-Al	1250	1720	1580
Ti-Ni	---	985	1310
Ti-Al	1325	1510	1510
Ni-Al	---	1380	1638

6.2 Alloying behaviour of milled powder samples of Fe-based HEAs

The diffraction pattern of the milled powder samples of HEA1, HEA2, and HEA3 with the milling time are illustrated in Figure 6.1(a), 6.2(a), and 6.3(a), respectively. The diffraction peaks corresponding to the elements i.e., Fe, Mn, Cr, Ti, Al, with and without Ni of pre-mixed are clearly evident in Figure 6.1(a), 6.2(a), and 6.3(a). As the milling progressed, it was ascertained that the elemental diffraction intensity started diminishing. At 10 h, the diffraction peaks at a higher angle, and Al has disappeared, which reflects that the Al has the highest alloying rate. After 20 h, the Ti, Ni and Cr peaks disappeared in the alloy systems with and without containing Ni. Alloying behaviour in the present HEAs was correlated with the elemental melting points, as elements with lower melting point (M.P.) diffuse faster as compared to those with higher melting point [107, 115]. After 30 h of milling, the dual-phase structures were formed i.e., BCC and χ-type phase structure. To achieve a more refined grain and homogenous solid solution, the milling was extended to 40 h. However, minor peak broadening and minor change in phase fraction were observed. After the mechanical alloying, the dual-phase structure of BCC (ferritic) as the major phase coexisted with χ-type phase (close to gamma brass structure) as the secondary phase in HEA1, HEA2, and HEA3, respectively was evident. Phase evolution during milling in the present Fe-based HEAs along the (110) planes in 2θ range from 42º- 46º, as illustrated in Figure 6.1(b), Figure 6.2(b), and Figure 6.3(b), respectively.

The variation of crystallite size (C.S.) and lattice strain (L.S.) at different milling times of 30 h, 35 h, and 40 h for the BCC phase and χ-type phase structure in the HEA1, HEA2, and HEA3, respectively were listed in Table 6.3. It was ascertained that the crystallite size of both phases is decrease with increase in milling time for HEA1, HEA2, and HEA3, and simultaneously lattice strain increases. Due to the atomic size mismatch and mechanical deformation in the powder

particles which leads to grain refinement in the powder particles and resultant increase in lattice strain during milling. The decrease in diffraction peak intensity and peak broadening during milling was due to the lattice distortion, which was induced during mechanical alloying. The dislocation density exhibited negligible changes with the milling time at 30 h, 35 h, and 40 h, this kind of observation was also observed in the previously reported HEAs [278, 284]. It was observed that the lattice parameters of BCC phase structures were decreases as the Ni content increases from x = 0 to 5 to 10 at. %. the HEA1, HEA2, and HEA3, and it is mentioned in Table 6.3.

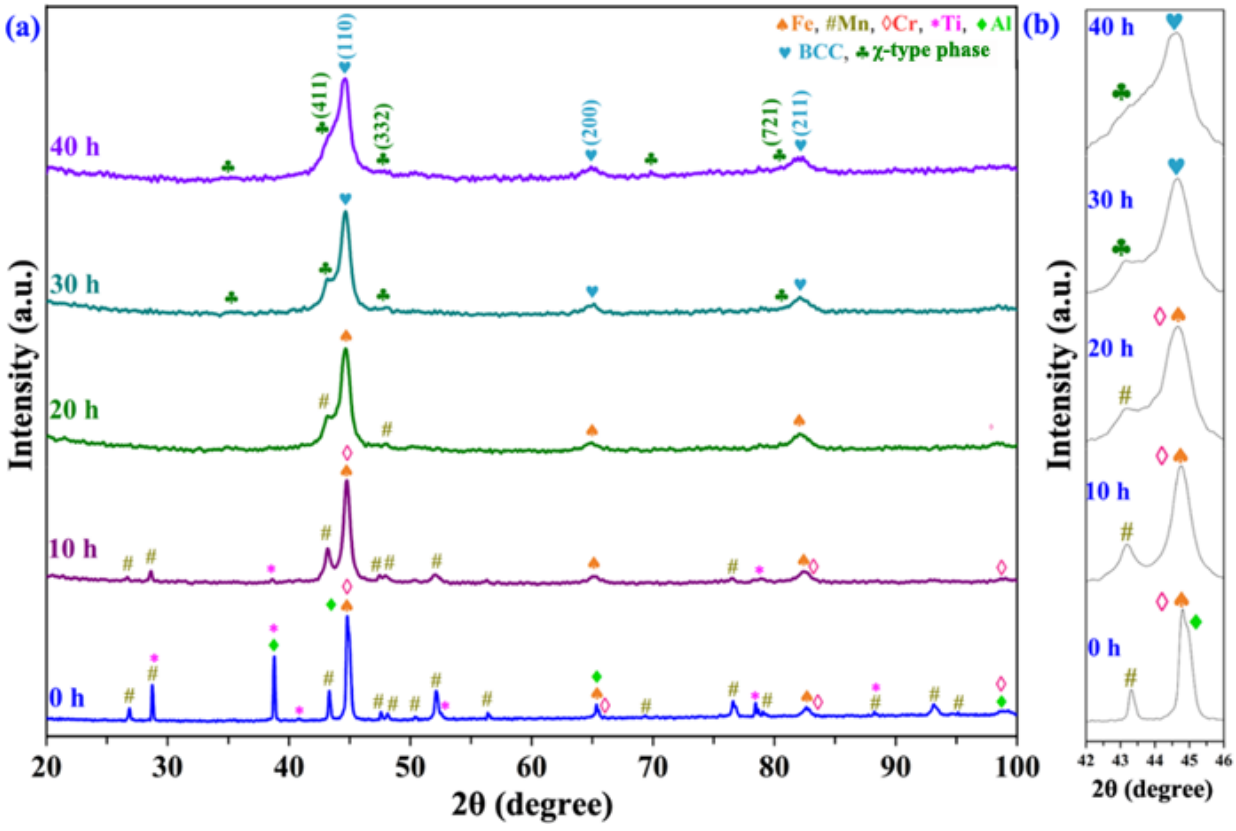

Figure 6.1: (a) Diffraction patterns of the milled powder of HEA1 samples at 0 h, 10 h, 20 h, 30 h and 40 h; (b) Enlarge view of the diffraction pattern in the range of 2θ = 42º- 46º. This shown the alloying behaviour of the elements with milling time, and finally forms the BCC and χ-type phase structure.

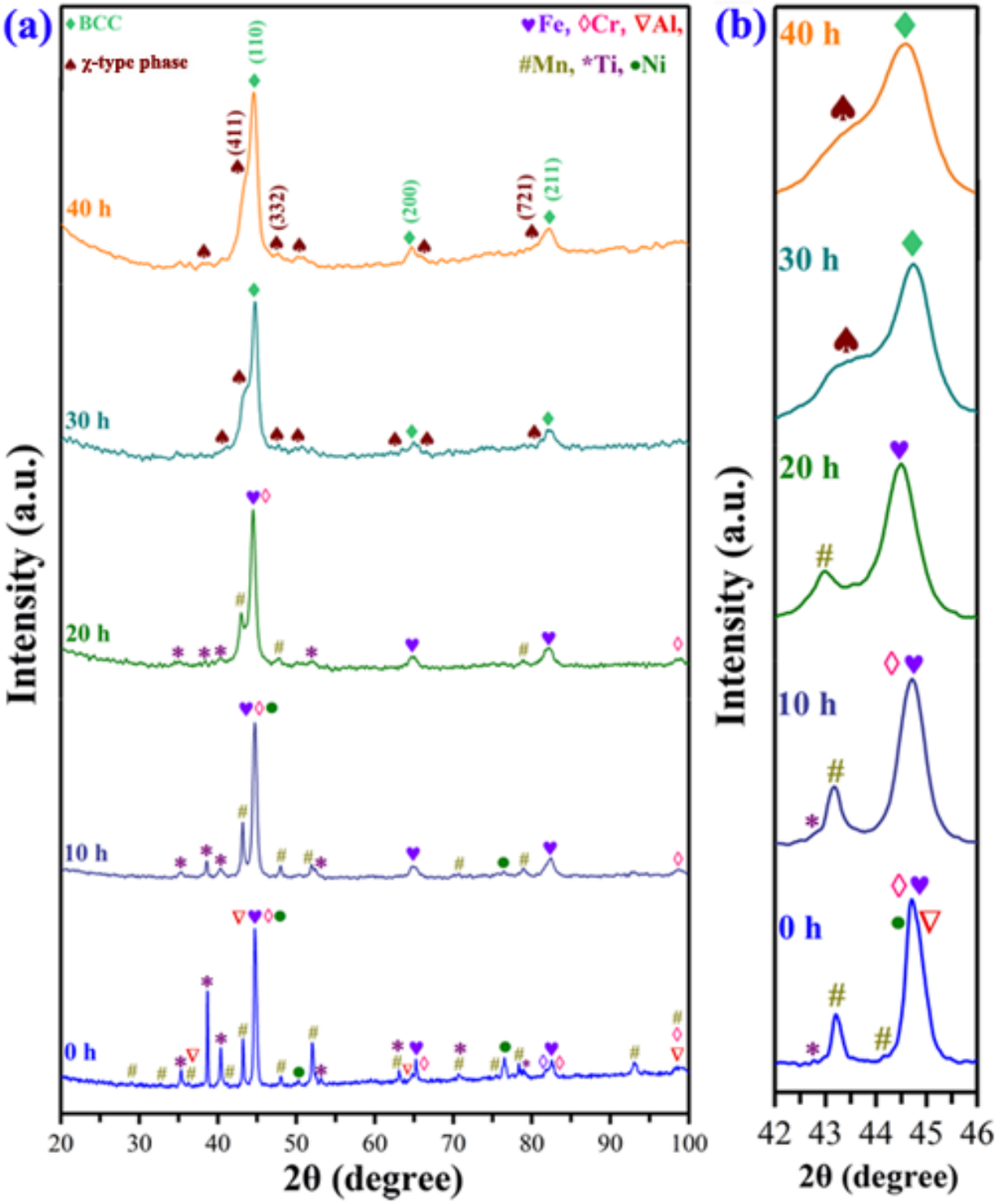

Figure 6.2: (a) Diffraction patterns of the milled powder samples of HEA2 at 0 h, 10 h, 20 h, 30 h and 40 h; (b) Enlarge view of the diffraction pattern in the range of 2θ = 42º-46º. This shows the dissolution of the elements with milling duration and finally forms the dual-phase structure consists of BCC and χ-type phase.

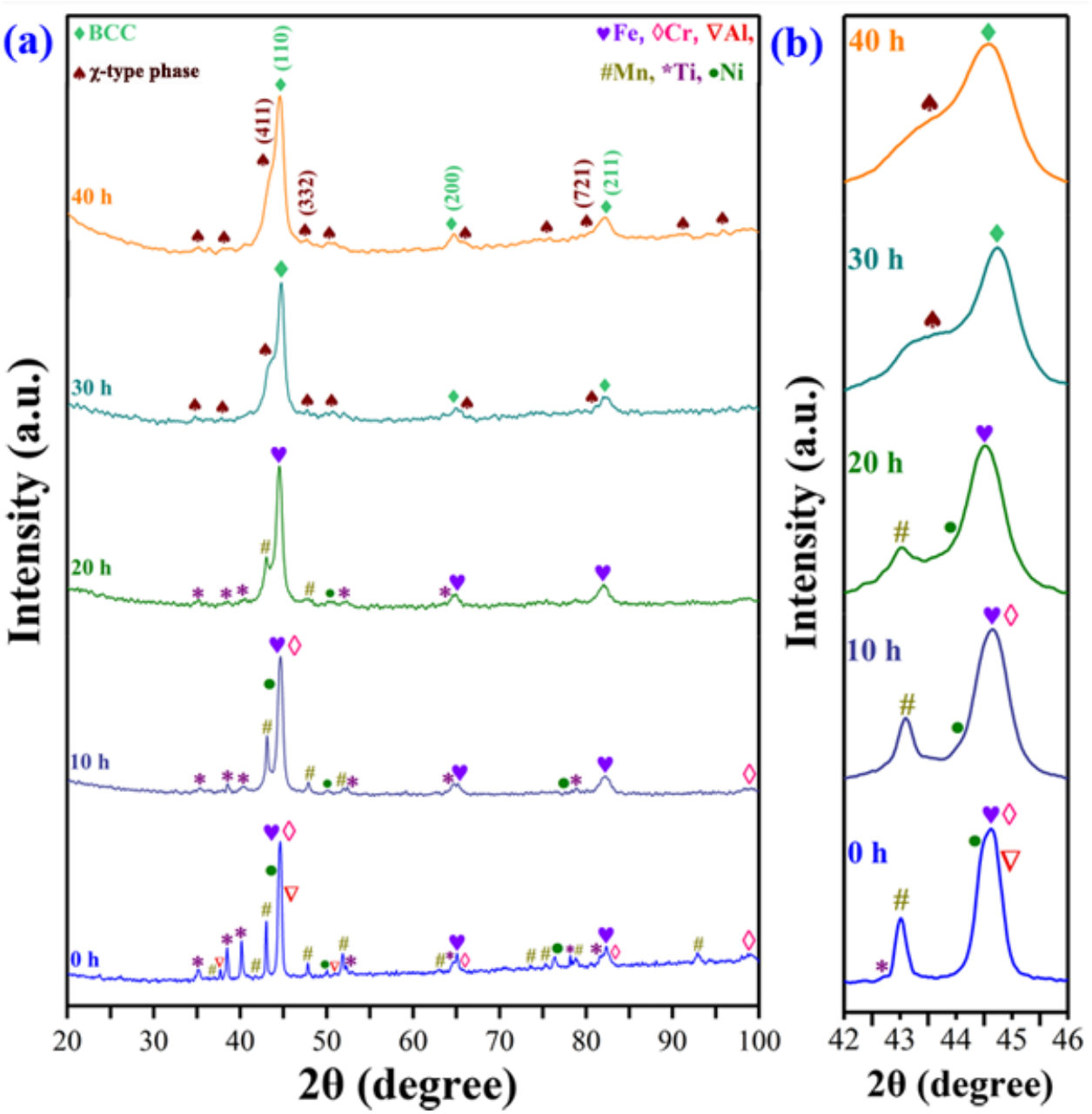

Figure 6.3: (a) Diffraction pattern of the milled powder sample of HEA3 at 0 h, 10 h, 20 h, 30 h and 40 h; (b) Enlarge view of the diffraction pattern in the range of 2θ = 42º- 46º. This displays the alloying behaviour of the elements with progress of milling, and at the end of milling its form the dual-phase structure contains of BCC and χ-type phase.

Table 6.3: Lattice parameter, phase fraction, crystallite size, microstrain, and dislocation density of Fe-based HEAs at 30 h, 35 h, and 40 h of milling time.

Milling duration	Phases formed	Alloys	Parameter				
			Lattice parameter (nm)	Phase fraction (%)	Crystallite size (nm)	Microstrain (%)	Dislocation density (m^{-2})
30 h	BCC	HEA1	0.2872	69	16	1.18	1.93×10^{18}
		HEA2	0.2869	73	17	1.22	1.88×10^{18}
		HEA3	0.2867	78	17	1.10	1.69×10^{18}
	χ-type phase	HEA1	0.8890	31	15	1.67	9.41×10^{17}
		HEA2	0.8889	27	16	1.82	9.62×10^{17}
		HEA3	0.8889	22	14	1.56	9.43×10^{17}
35 h	BCC	HEA1	0.2872	69	16	1.18	1.93×10^{18}
		HEA2	0.2869	73	17	1.22	1.88×10^{18}
		HEA3	0.2867	78	17	1.10	1.69×10^{18}
	χ-type phase	HEA1	0.8890	31	15	1.67	9.41×10^{17}
		HEA2	0.8889	27	16	1.82	9.62×10^{17}
		HEA3	0.8889	22	14	1.56	9.43×10^{17}
40 h	BCC	HEA1	0.2872	69	16	1.18	1.93×10^{18}
		HEA2	0.2869	73	17	1.22	1.88×10^{18}
		HEA3	0.2867	78	17	1.10	1.69×10^{18}
	χ-type phase	HEA1	0.8890	31	15	1.67	9.41×10^{17}
		HEA2	0.8889	27	16	1.82	9.62×10^{17}
		HEA3	0.8889	22	14	1.56	9.43×10^{17}

6.3 Morphology analysis and chemical analysis of Fe-based HEAs

The SEM micrographs of the milled powder samples of HEA1, HEA2, and HEA3 at different milling time are shown in Figure 6.4, 6.5 and 6.6(a-d), respectively, which show the powder

particle size, shape and morphology. 10 h milled powder particles were of different sizes and shapes, and it is randomly disturbed in these alloy systems. The powder particles became more homogenous as milling time increased, and it is evident from Figure 6.4, 6.5, and 6.6(a-d).

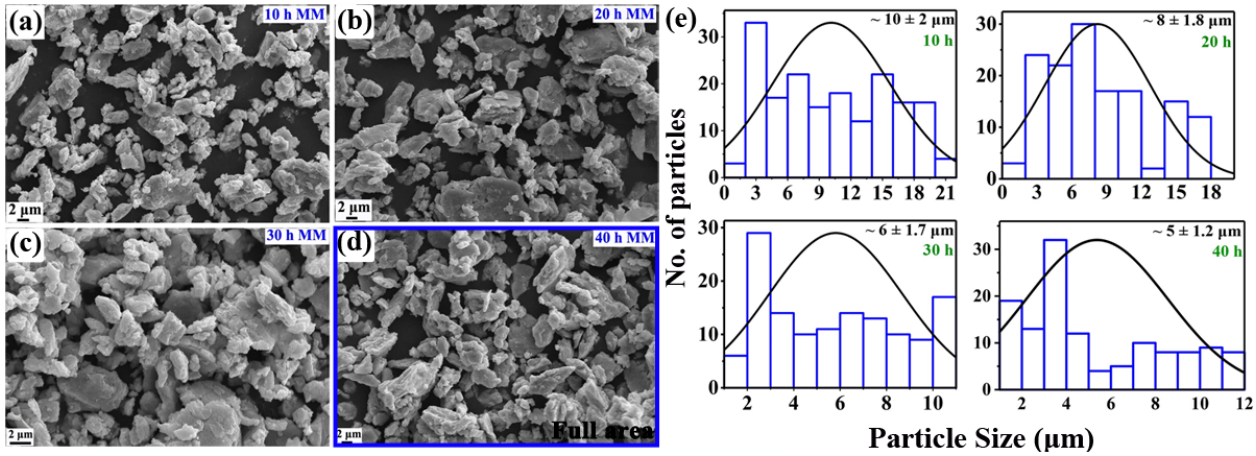

Figure 6.4: (a-d) The microstructural features of the milled powder samples at 10 h, 20 h, 30 h and 40 h of the HEA1; (e) The particle size distribution (histogram plot) of the alloy at 10 h, 20 h, 30 h and 40 h. The size of the particles and average particle size are decreasing with the increase in milling time and it is clearly visible in the histogram plot.

The full area EDS analysis of the 40 h milled sample was done, which is marked in Figure 6.4, 6.5, and 6.6(d), and its values are listed in Table 6.4. These show the presence of all the elements and chemical homogeneity in powder samples of Fe-based HEAs. The particle size distribution at different milling times i.e., 10 h, 20 h, 30 h, and 40 h, are shown in the histogram in Figure 6.4, 6.5, and 6.6(e) for HEA1, HEA2, and HEA3, respectively. The average particle size was calculated using the ImageJ software. Area elemental mapping of the 40 h green pellet samples of the HEA1, HEA2, and HEA3 was done, which is displayed in Figure 6.7, 6.8, and 6.9, respectively. This also ascertained that the dual-phase structure was formed after the milling by showing different contrast features in all the elemental mapping. The elemental mapping of Fe has shown the two-contrast

region i.e., Fe-rich contrast which corresponds to the BCC phase, and the lean contrast region is related with the χ-type phase (rich in Mn, Cr, and Ti).

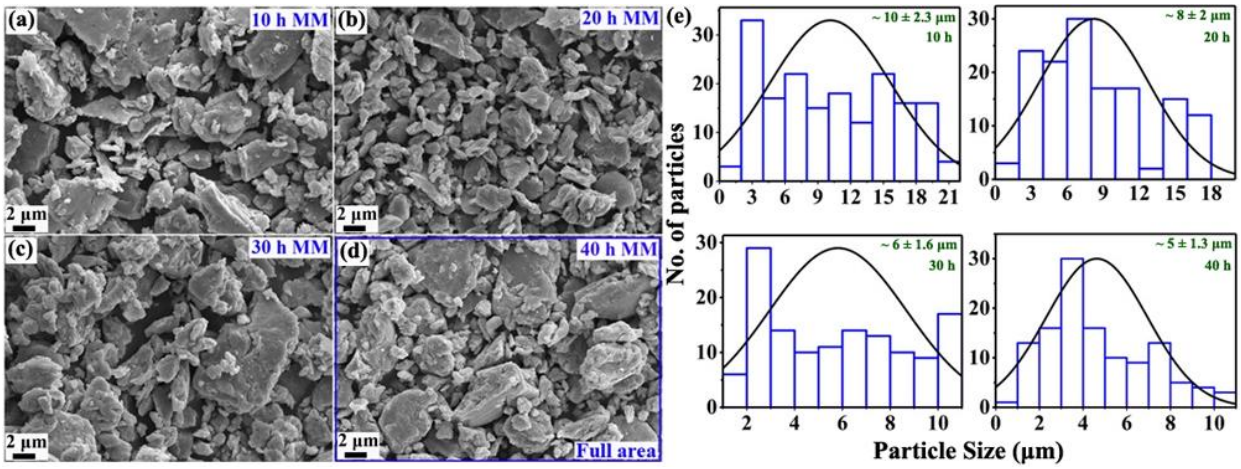

Figure 6.5: (a-d) The microstructural features of the milled powder samples at 10 h, 20 h, 30 h and 40 h of the HEA2; (e) The particle size distribution (histogram plot) of the alloy at 10 h, 20 h, 30 h and 40 h. The decrease in particle size and average particle size with the increase in milling time is clearly visible in the histogram plot.

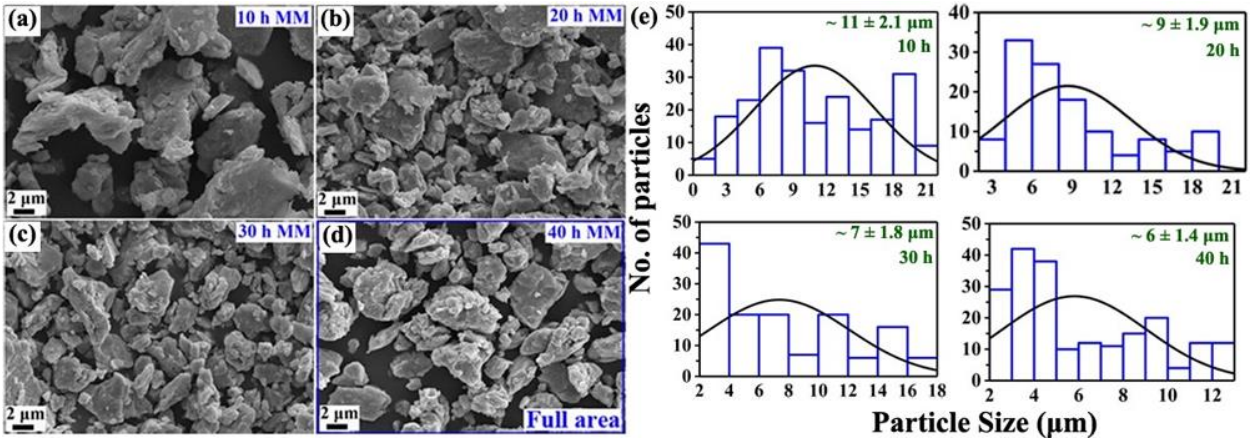

Figure 6.6: (a-d) The microstructural features of the milled powder samples at 10 h, 20 h, 30 h and 40 h of the HEA3; (e) The particle size distribution (histogram plot) of the alloy at 10 h, 20 h, 30 h and 40 h. The size of the particles and average particle size are in decreasing trend as the milling time is increases and this trend is clearly visible in the histogram plot.

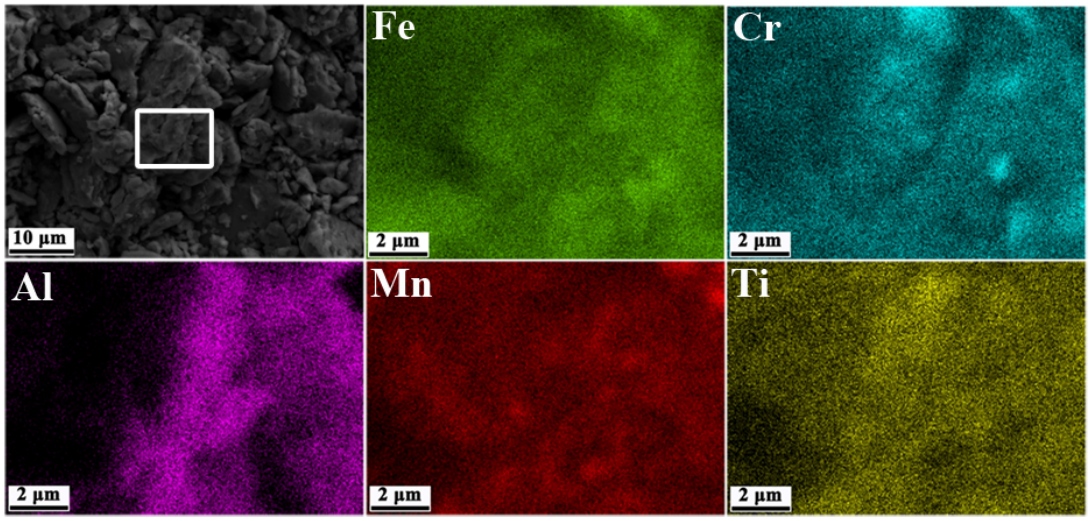

Figure 6.7: Elemental mapping of the 40 h green pellet of the HEA1. This illustrates the two-contrast region i.e.; one is Fe rich (BCC phase) and another is Cr and Ti rich (χ-type phase).

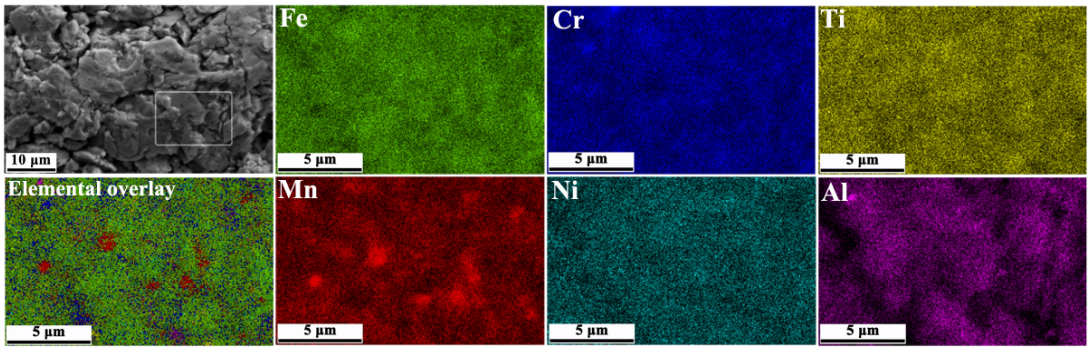

Figure 6.8: Elemental mapping of the 40 h green pellet of the HEA2. This illustrates the two-contrast region i.e.; one is Fe rich (BCC phase) and another is Mn, Cr and Ti rich (χ-type phase).

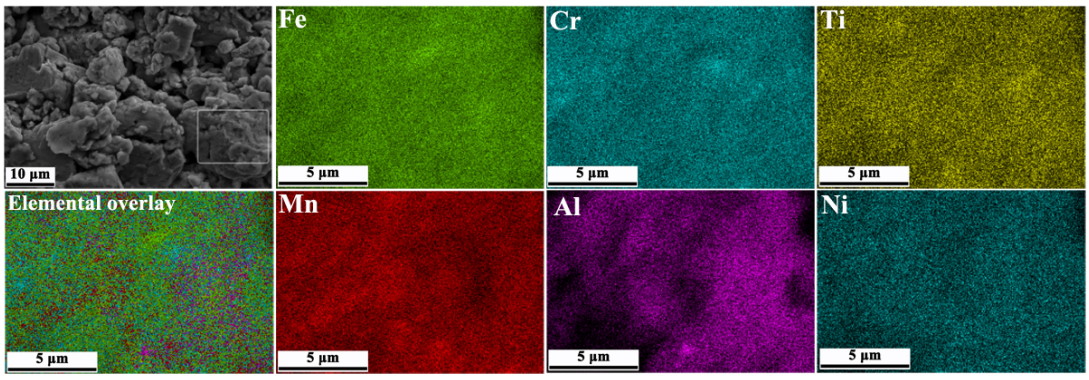

Figure 6.9: Elemental mapping of the 40 h green pellet of the HEA3. This illustrates the two-contrast region i.e.; one is Fe rich (BCC phase) and another is Mn, Cr and Ti rich (χ-type phase).

Table 6.4: Full area EDS analysis of Fe-based HEAs.

Elemental composition (at. %)							
Sample condition	**Sample designations**	**Fe**	**Mn**	**Cr**	**Ni**	**Ti**	**Al**
Powder sample	**HEA1**	40.82	19.38	19.56	---	9.56	10.68
	HEA2	41.14	18.92	15.82	5.38	10.23	8.51
	HEA3	40.63	20.43	10.33	10.32	9.71	8.78

6.4 Thermal stability of the as-milled powder samples

Figure 6.10(a, b, and c) shows the DSC curve of the 40 h milled powder sample of the HEA1, HEA2, and HEA3, respectively, heated in the range of 200 ℃ to 1000 ℃. The DSC curves reveal the exothermic event at 500 ℃, 540 ℃, and 510 ℃ for HEA1, HEA2, and HEA3, respectively. The exothermic event depicts the phase transformation occurred at elevated temperature. To correlate the exothermic events, the ex-situ XRD of the annealed powder sample was done at 400 ℃, and 600 ℃ for all the three alloy systems. The diffraction pattern of various annealed samples of HEA1, HEA2, and HEA3 is shown in Figure 6. 11(a), 6. 12(a), and 6. 13(a), respectively. The Fe-based HEAs are thermally stable up to 400 ℃, and in between 500 ℃ to 600 ℃, the FCC solid solution was evolved, which is confirmed by the ex-situ XRD of the annealed sample at 600 ℃ in all three alloy systems. The enlarged view in between the 2θ (42º- 46º) for HEA1, HEA2, and HEA3 is shown in Figure 6. 11(b), 6. 12(b), and 6. 13(b), respectively. The Rietveld refinement of the annealed samples at 400 ℃, and 600 ℃ was done to evaluate the lattice parameter, C.S., L.S., and phase fraction, and it is listed in Table 6.5.

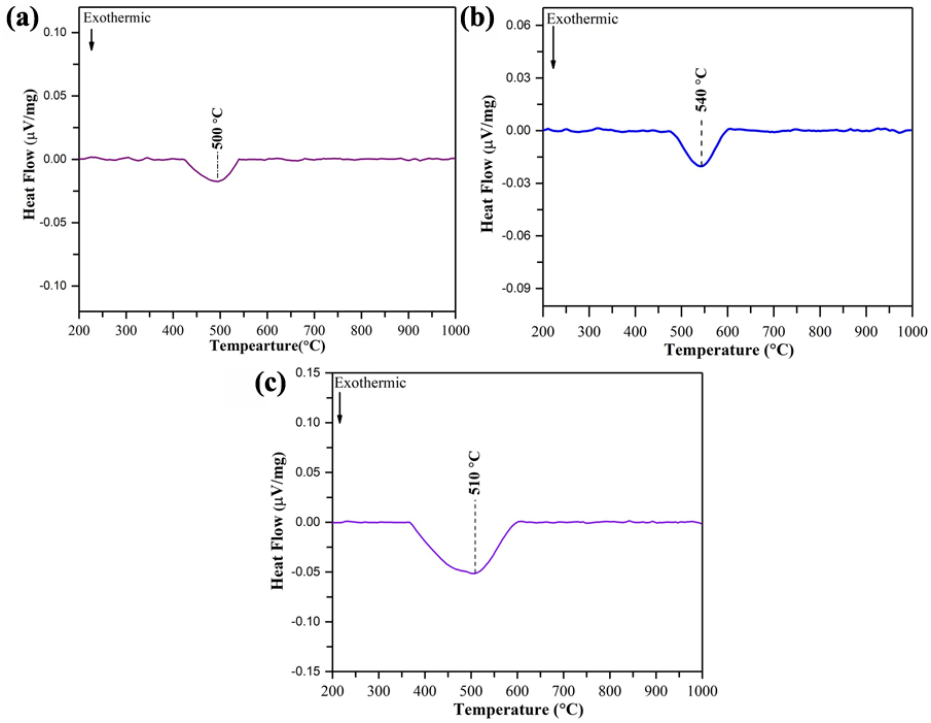

Figure 6.10: (a, b and c) DSC curve of the 40 h milled sample of the HEA1, HEA2, and HEA3, respectively in between 200 °C to 1000 °C. This curve shows the exothermic events at 500 °C, 540 °C and 510 °C for HEA1, HEA2 and HEA3, respectively.

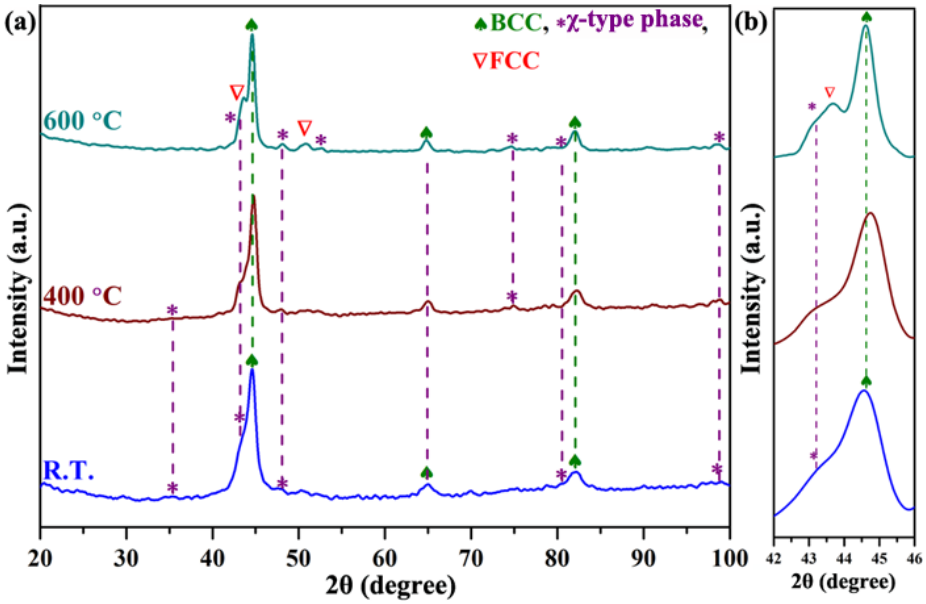

Figure 6.11: (a) Diffraction pattern of the 25 °C, and annealed samples of HEA1 at 400 °C and 600 °C; (b) Enlarged view in the 2θ range from 42º- 46º. The formation of FCC solid solution was correlated with exothermic events at 500 °C.

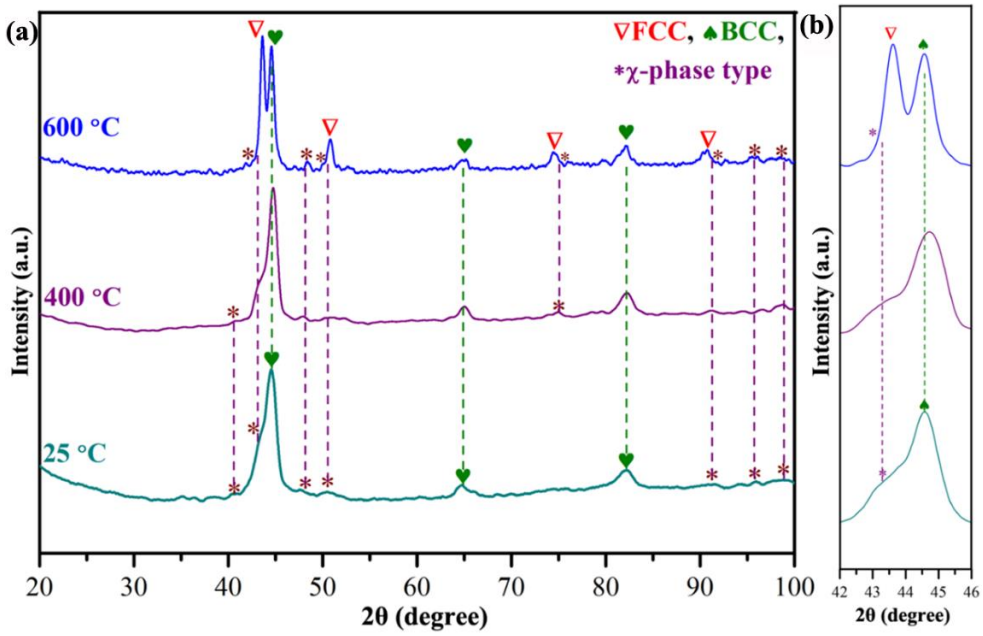

Figure 6.12: (a) Diffraction pattern of the 25 ℃, and annealed samples of HEA2 at 400 ℃ and 600 ℃; (b) Enlarged view in the 2θ range from 42º- 46º. The formation of FCC solid solution was associated with exothermic events at 540 ℃.

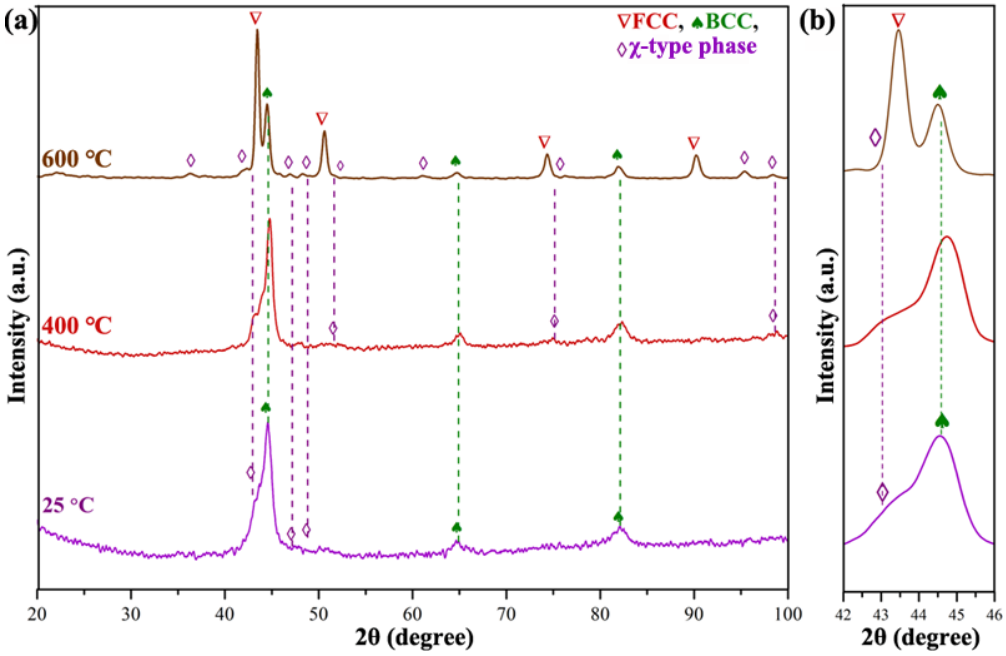

Figure 6.13: (a) Diffraction pattern of the 25 ℃, and annealed samples of HEA3 at 400 ℃ and 600 ℃; (b) Enlarged view in the 2θ range from 42º- 46º. The formation of FCC solid solution was linked with exothermic events at 510 ℃.

Table 6.5: The values of the structural and microstructural parameters of the annealed and SPSed samples of the HEA1, HEA2, and HEA3.

Sample conditions	Phases formed	Alloys	Lattice parameter (nm)	Phase fraction (%)	Crystallite size (nm)	Microstrain (%)
400 °C	BCC	HEA1	0.2872	75.20	31	0.73
		HEA2	0.2870	63.20	20	0.66
		HEA3	0.2869	60.0	23	0.72
	χ-type phase	HEA1	0.8890	24.80	18	7895
		HEA2	0.8889	36.80	16	0.74
		HEA3	0.8889	40.0	19	0.90
600 °C	BCC	HEA1	0.2870	59.60	48	4844
		HEA2	0.2869	41.50	24	0.54
		HEA3	0.2867	29.0	26	0.61
	FCC	HEA1	0. 3630	25.40	31	8679
		HEA2	0.3628	48.20	21	0.49
		HEA3	0.3624	59.0	28	0.72
	χ-type phase	HEA1	0.8890	15.0	23	0.52
		HEA2	0.8889	10.30	20	0.65
		HEA3	0.8889	12.0	23	0.79
SPSed	BCC	HEA1	0.2870	72.00	43	0.25
		HEA2	0.2869	32.0	38	0.28
		HEA3	0.2867	11.0	25	0.28

	FCC	HEA1	0. 3630	20.00	24	0.52
		HEA2	0.3628	61.0	41	0.37
		HEA3	0.3624	79.0	52	0.29
	χ-type phase	HEA1	0. 8890	8.00	17	2310
		HEA2	0.8889	7.0	27	0.22
		HEA3	0.8887	10.0	24	0.38

6.5 Structural and microstructural analysis of SPSed samples of Fe-based HEAs

Figure 6.14(a, b, and c) display the diffraction patterns of the SPSed samples of HEA1, HEA2, and HEA3 at 900 ℃ and 50 MPa, which mostly consist the dual-phase structure of BCC and FCC along with the χ-type phase as precipitates. The Rietveld refinement of the XRD pattern of HEA1, HEA2, and HEA3 confirmed the formation of dual-phase structure along with the precipitates, which is illustrated in Figure 6.15(a, b, and c). The BCC (major) to BCC + FCC to FCC rich phase transformation was observed as Ni content increased from x = 0 to 5 to 10 at. %. The lattice parameter, phase fraction, crystallite size and microstrain of the SPSed of Fe-based HEAs are mentioned in Table 6.5. It was observed from the Table 6.3 that the lattice parameter decreases with the variation of the Ni content from x= 0 to 10 at. %. Figure 6.16(a, b, and c) show the SEM (BSE) micrographs of the SPSed sample of Fe-based HEAs. Figure 6.16(a) illustrates the different contrasts i.e., light and dark grey, which correspond to the FCC and BCC phases, respectively. Figure 6.16(b and c) illustrates the different contrasts i.e., light and dark grey, which correspond to the BCC and FCC phases, respectively. The point and full area analysis of the SPSed samples of Fe-based HEAs were done, and it is marked as 1 and 2 in the SEM micrographs (Figure 6.16(a, b, and c)). The values of the full and point EDS analysis of the SPSed sample of Fe-based HEAs

are listed in Table 6.6. The chemical analysis also confirmed the dual-phase formation in SPSed samples, which shows that the BCC phase is rich in Fe and Cr, and the FCC phase is rich in Fe and Mn. Area elemental mapping of the SPSed samples of the HEA1, HEA2, and HEA3 is displayed in Figure 6.17(a, b, and c), respectively. It was evident from the elemental mapping of the SPSed sample that the FCC phase is rich in Fe, Mn, and Ni, and the BCC phase is rich in Fe and Cr. This observation also confirmed the dual-phase formation in the Fe-based HEAs.

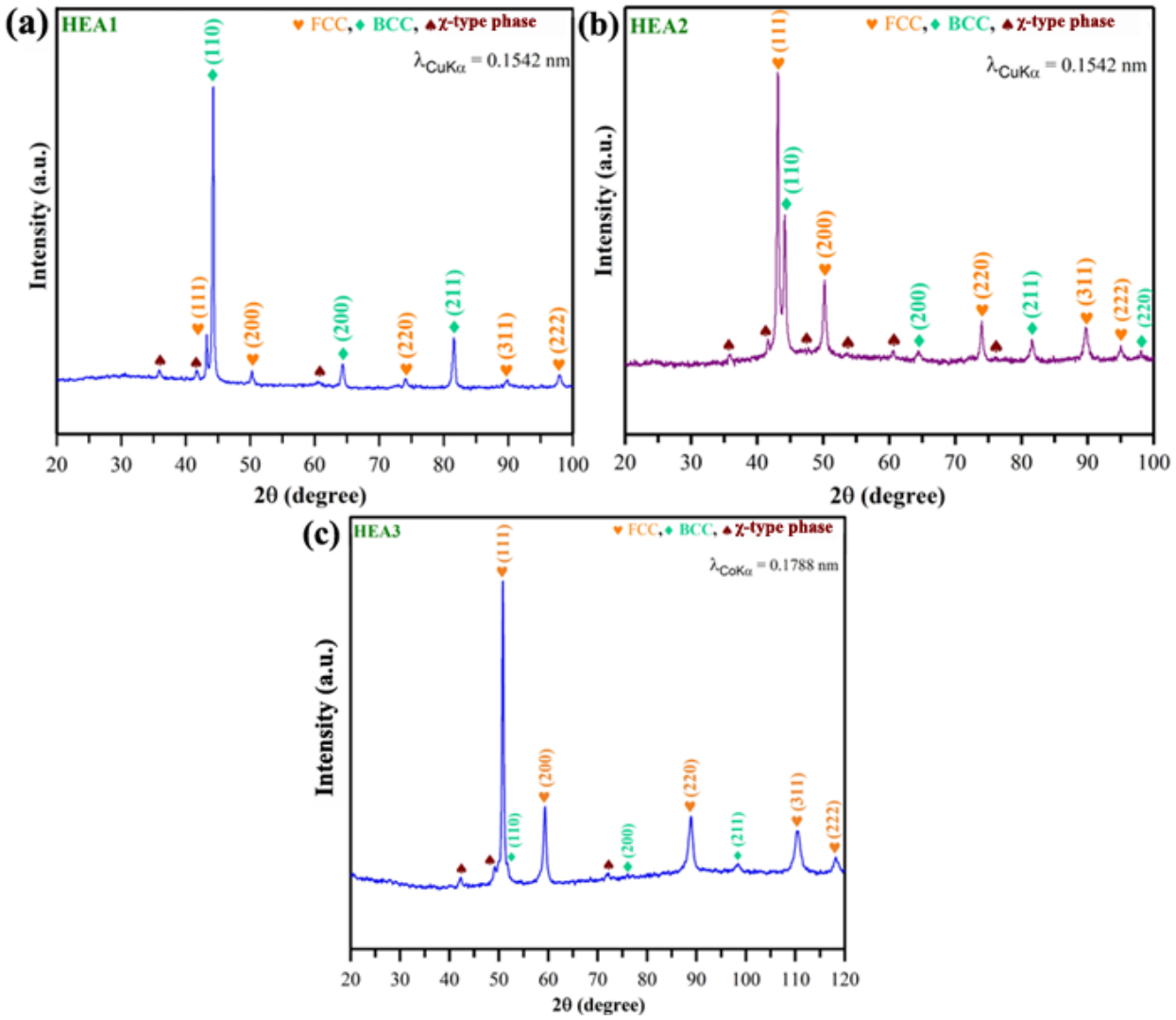

Figure 6.14: (a, b, and c) Diffraction pattern of the spark plasma sintered sample of HEA1, HEA2, and HEA3, respectively. This shows the formation of BCC and FCC phase in SPSed sample.

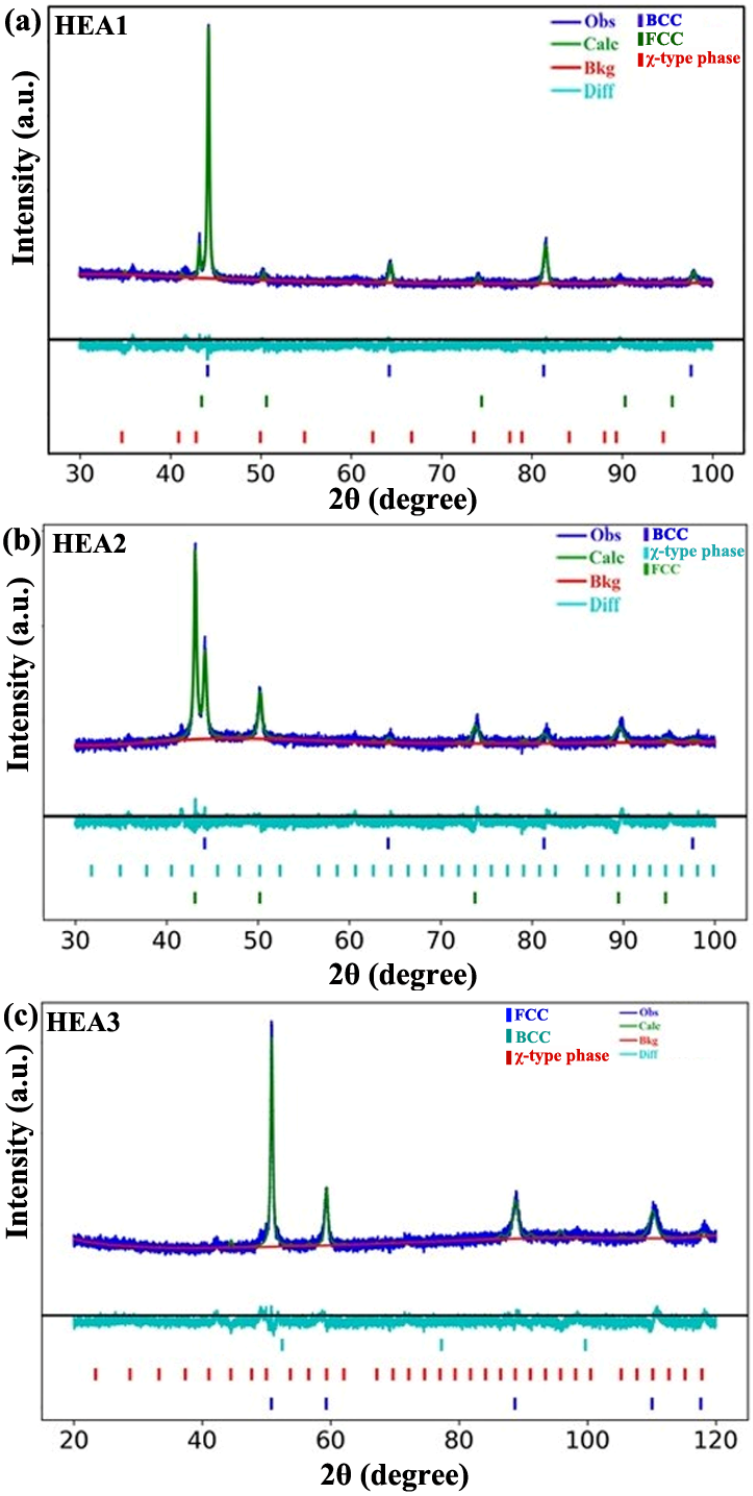

Figure 6.15: (a, b, and c) Rietveld refinement of the SPSed of HEA1, HEA2, and HEA3, respectively. This also confirms the formation of BCC and FCC along with χ-type phase as precipitates.

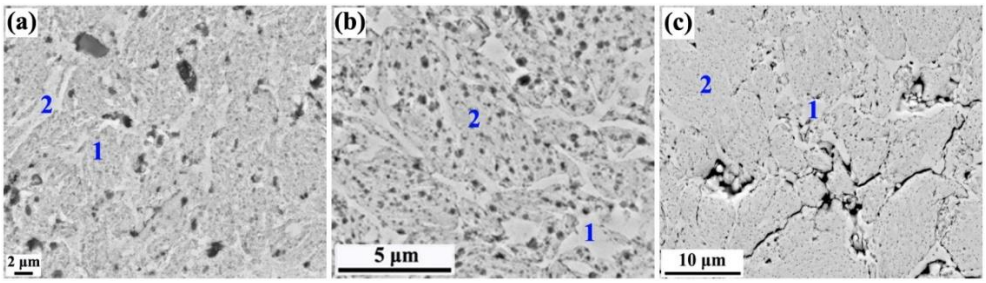

Figure 6.16: (a, b, and c) The microstructural features (SEM-BSE) of the SPSed sample of HEA1, HEA2, and HEA3, respectively. This shows the two contrast features i.e., light and dark grey, which correspond with the BCC and FCC phase. The light and dark contrast fetaures are marked as 1 and 2 for point EDS analysis.

Table 6.6: Full area and point EDS analysis of the HEA1, HEA2, and HEA3 after the SPS.

Sample condition		Elemental composition (at. %)						
		Scan area	Fe	Mn	Cr	Ni	Ti	Al
SPSed sample	HEA1	Full area	41.0	20.0	19.0	---	11.0	9.0
		Spot 1 (FCC)	**48.21**	26.42	15.68		3.67	6.02
		Spot 2 (BCC)	**44.04**	12.90	23.0	---	14.53	5.53
	HEA2	Full area	40.70	19.20	5.10	15.20	10.7	9.0
		Spot 1 (BCC)	**45.40**	9.59	19.12	3.13	12.97	9.79
		Spot 2 (FCC)	**49.57**	19.10	8.81	11.66	6.14	4.72
	HEA3	Full area	41.10	19.10	9.30	11.20	10.1	9.2
		Spot 1 (FCC)	**49.42**	18.02	9.44	16.82	2.54	3.76
		Spot 2 (BCC)	**42.70**	11.60	16.99	4.40	13.21	11.10

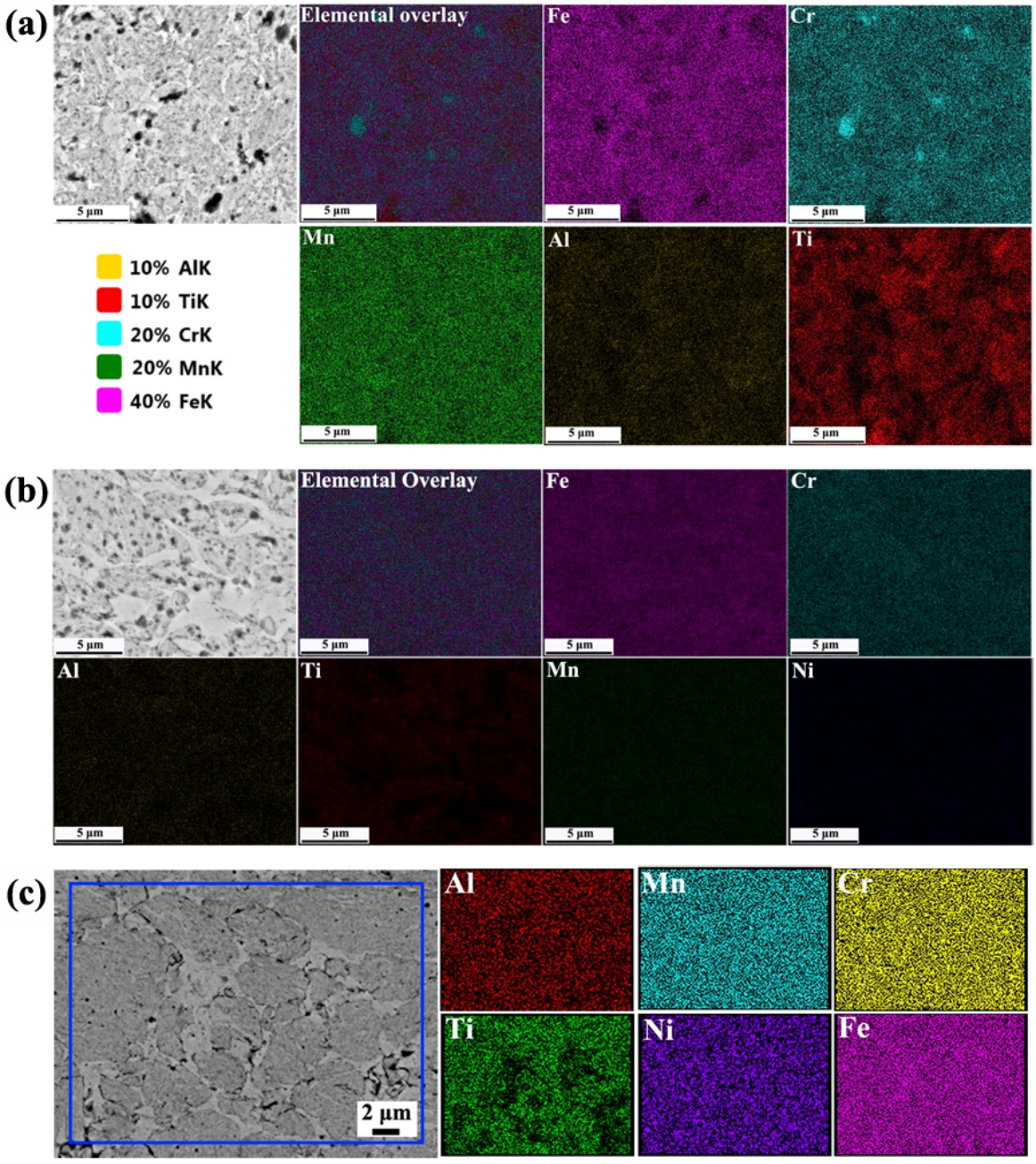

Figure 6.17: (a, b and c) Elemental mapping of the SPSed sample of HEA1, HEA2, and HEA3, respectively.

6.6 Physical and mechanical properties of the SPSed samples of Fe-based HEAs

Figure 6.18(a) illustrates the indentation load vs depth of indentation curves of the SPSed sample of Fe-based HEAs. Figure (a1, a2, and a3) show the indentation spot (optical image) of the

corresponding indentation curve of the Fe-based HEAs. The optical micrograph does not show any crack formation at 5000 mN in the present alloy systems. The depth of indentation at 5000 mN was found to be 5.8 μm, 6.4 μm, and 7.1 μm, for HEA1, HEA2, and HEA3, respectively. The microhardness and elastic constant decreases from 6.4 GPa to 4.2 GPa and 183 GPa to 127 GPa as the Ni content (x = 0 to 10 at. %) increases. The engineering stress vs strain curve under the compressive load of the SPSed sample of Fe-based HEA is shown in Figure 6.18(b). The decrease in compressive yield strength and increase in compressive strain were observed as the Ni content increased from x = 0 to 10 at. % and its value is mentioned in Table 6.7. The decrease in yield strength and microhardness is due to the phase transformation from BCC to FCC as the Ni content increases from x = 0 to 10 at. %. This kind of increase in ductility and decrease in strength was also observed in previously reported HEAs when the structure transformed from BCC to FCC and vice-versa [156, 158, 164]. It can be pointed out that BCC phase is hard and less ductile than that of the FCC phase, which is stabilized due to increase in Ni.

SEM micrographs of the fractured SPSed samples after the compression test are shown in Figure 6.19. The SEM micrograph of HEA1 discerned the microcrack and brittle fracture kind of features. The initiation of microcrack may be started from brittle χ-type phase precipitates and FCC grains due to the modulus mismatch between the two phases. The brittle fracture is the dominant fracture in case of HEA1, as BCC structure is the major phase in the SPSed sample. In HEA2 the dominant fractured mechanism is ductile and brittle both because it was observed from the fractography (as shown in Figure 6.19) that the river kind of features and shallow dimples are present. The HEA3 fractography shows the shallow dimple features are evenly disturbed in the fractured surfaces, this corresponds that the ductile fracture is dominant. The presence of micro

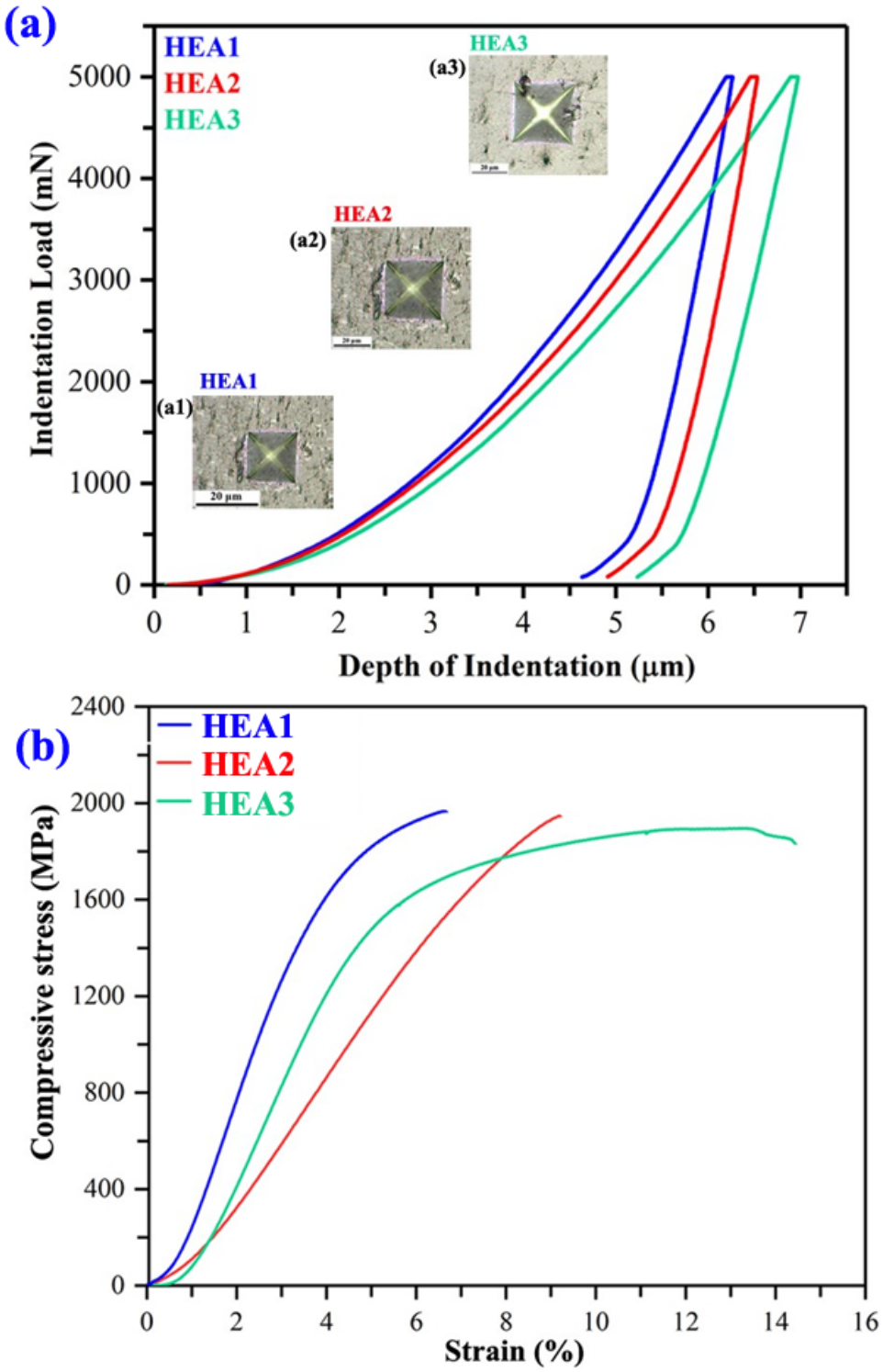

Figure 6.18: (a) Depth of penetration Vs Indentation load; (b) compressive engineering stress and strain curve; (a1, a2, and a3) Optical micrograph of the corresponding indentation spot of the HEA1, HEA2, and HEA3, respectively.

Table 6. 7: Physical, mechanical and wear prperties of the SPSed samples of Fe-based HEAs.

Designation	Density (g/cc)	Hardness (GPa)	Elastic modulus (GPa)	Yield strength (MPa)	Strain (%)	CoF	Specific W. R. (mm^3/mN)
HEA1	6.52	6.4	183	1962	6.2	0.2	1.30×10^{-4}
HEA2	6.61	5.7	131	1810	11.7	0.48	1.65×10^{-4}
HEA3	6.80	4.2	127	1300	15.8	0.47	4.21×10^{-4}

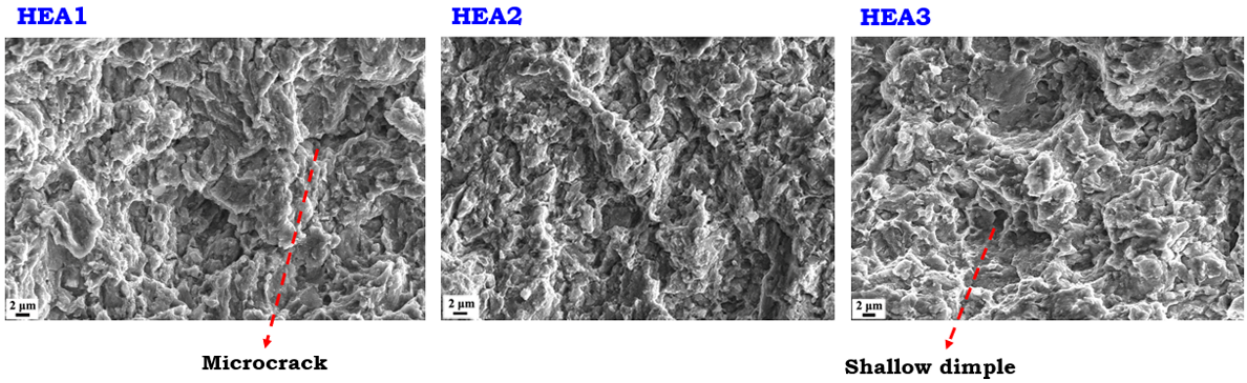

Figure 6.19: The microstructural features (SEM-SE) of the fractured surfaces after the compression test of the HEA1, HEA2, and HEA3, respectively.

pores present in all the three fractured micrographs are of same size of nanoprecipitates (χ-type phase) as observed in the SEM micrograph of the SPSed samples (as shown in Figure 6.16).

6.7 Wear behaviour of the SPSed samples of Fe-based HEAs

It can be observed from Figure 6.20(a, b, and c) that the coefficient of friction (CoF) curves at 5 N, 10 N, and 20 N of the Fe-based HEAs demonstrate different sawtooth behaviours. The most and gradual fluctuation is in the case of HEA2 and HEA1, respectively. The fluctuations in CoF curves in the HEAs are associated with the microhardness, microstructure uniformity of the alloy,

wear debris, crack formation, glaze layer, and oxide fragments during dry friction [288]. In the present alloy systems, the microstructures are relatively homogeneous and all have the dual

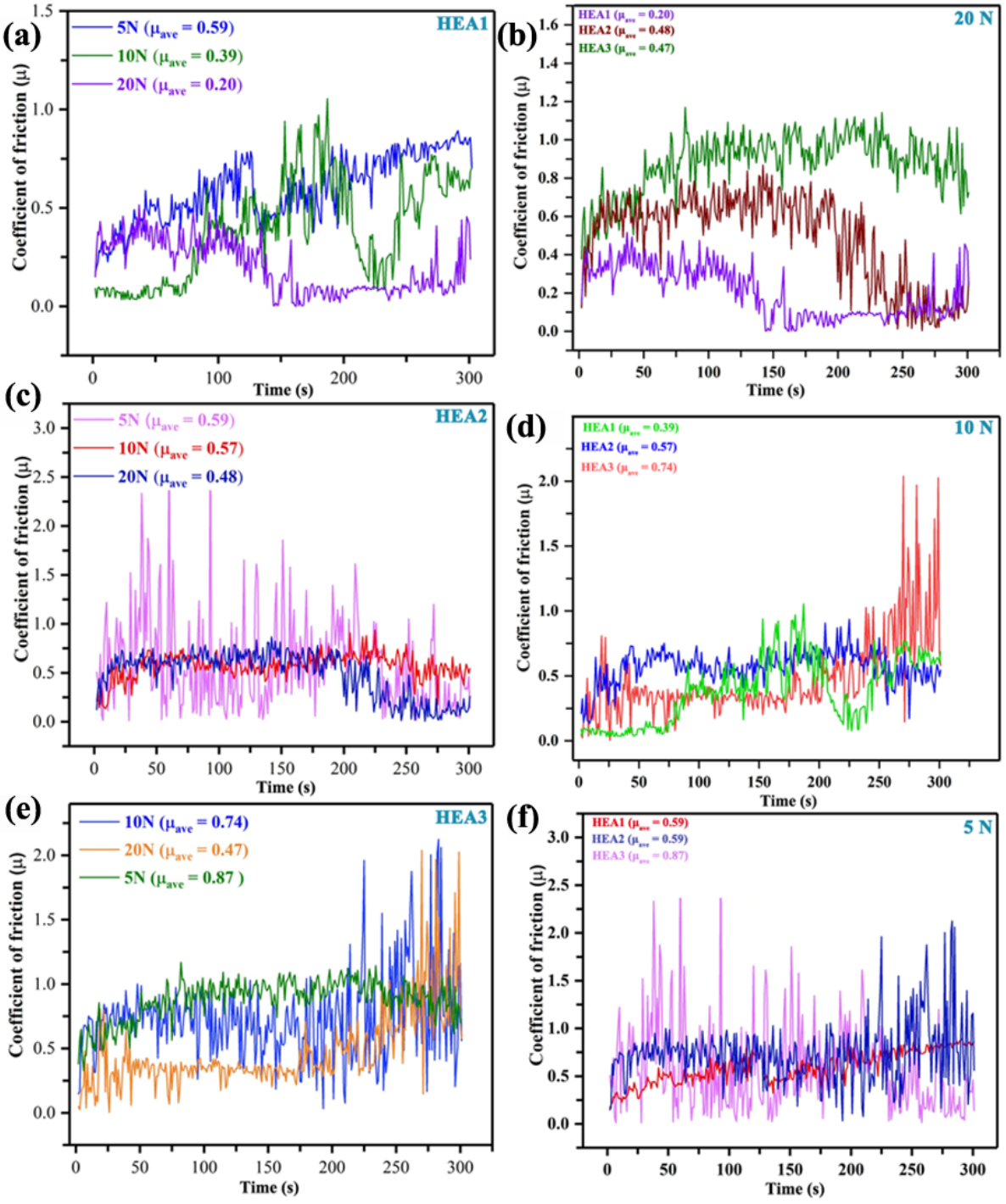

Figure 6.20: (a, b, and c) Curve between coefficient of friction vs time for the HEA1, HEA2, and HEA3, respectively; (d, e, and f) Coefficient of friction vs time at 20 N, 10 N, and 5 N, respectively.

phase structure, that's why there is no consequence of microstructural inhomogeneity on the CoF [288, 289]. The reason why the wear coefficient fluctuates greatly at lower load conditions is due to the progressive wear, wear debris, and formation of local cracks on the worn surface, which will cause the sharp rise of the CoF. The effect of the counter hardball (Al_2O_3) has a high impact on the opposite surface (HEAs) as the load increases. At higher loads, an abrasive ball easily removes the material as it sinks more in the surface. This effect is reduced as the microhardness of the HEAs increases, as the surface becomes harder and its exhibits higher resistance against the abrasive ball. This type of behaviour is evident from the comparative CoF curve of Fe-based HEAs with time at different load condition is shown in Figure 6.20(d, e, and f). The high CoF at the early period of the test is due to the low contact area between the counter ball and sample resultant high pressure between the contact area. The specific wear rate of Fe-based HEAs is inversely proportional to the microhardness value of the alloys. As the microhardness is decreased the specific wear rate is increased, this happens due to the phase transformation from hard BCC-rich phase to soft FCC-rich phase in the present alloy systems.

Figure 6.21(a, b, and c) SEM micrographs display the worn surface features of the HEA1 at load conditions of 5 N, 10 N, and 20 N, respectively, which exhibits the abrasive kind of wear mechanism as its shows the grooves, accumulation of wear debris, pits, microcracks, and spalling features. The worn surface features demonstrated that at higher load conditions worn surface is severely affected as compared to lower load conditions, that's why at higher load conditions specific wear rate is higher. Due to the accumulation of wear debris on the worn surface, the fluctuation in CoF is more at lower load conditions, which is observed in Figure 6.20(f) for all the present alloy systems. The worn surface features of the HEA2 at load conditions of 5 N, 10 N, and 20 N are illustrated in Figure 6.21(d, e, and f), respectively. This shows the scratch,

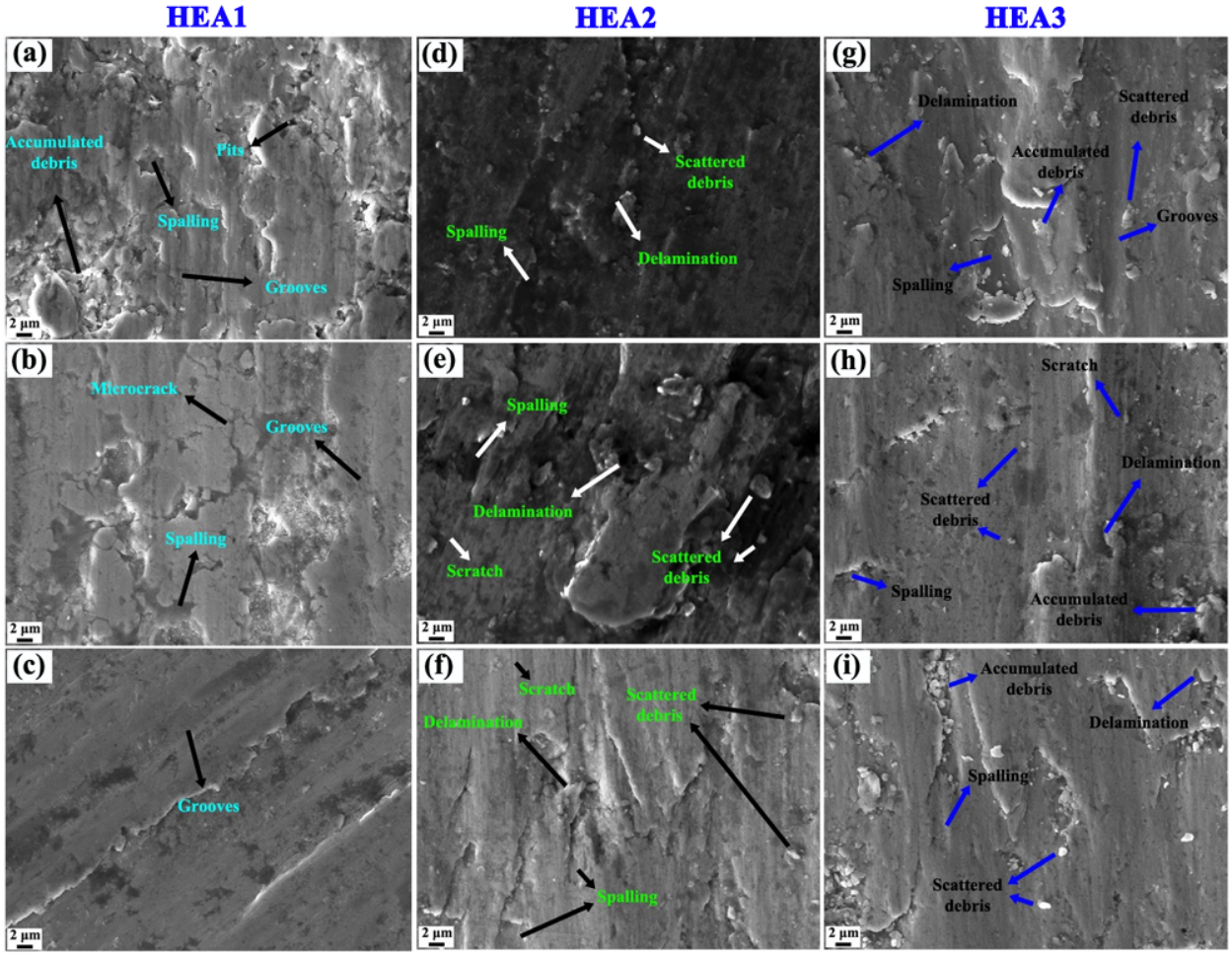

Figure 6.21: (a, b, and c) SEM (SE) of the worn surface features of the HEA1 at 5 N, 10 N, and 20 N load conditions, respectively; (d, e, and f) HEA2 at 5 N, 10 N, and 20 N, respectively; (g, h, and i) HEA3 at 20 N, 10 N, and 5 N, respectively.

scattered debris, delamination, and spalling features, most of the features are abrasive wear mechanisms. This alloy showed the same kind of behaviour at different load conditions as in HEA1. Figure 6.21(g, h, and i) shows the SEM image of the worn surface of the HEA3 at 20 N, 10 N, and 5 N load conditions, respectively. These alloys also showed the abrasive wear mechanism is the dominant mechanism and the wear behaviour at different load conditions as the previous HEA1 and HEA2.

6.8 Biocompatibility of the SPSed samples of Fe-based HEAs

The biocompatibility MTT-assay test of the SPSed sample of HEA1, HEA2, and HEA3 with 316L stainless steel as control is performed under Osteosarcoma MG-63 cell for 3, 5, and 7 days, as displayed in Figure 6.22. The optical absorbance value was measured directly from the living cell viability at a wavelength of 595 nm using the equation no. 2.6. The cell viability of the Fe-based HEAs and control samples increases with the increase of the incubation period. During the initial period of the incubation period of 3 and 5 days, the mean optical density ($p \leq 0.05$) was not much in the high entropy steel surface, relative to the control. However, for the incubation period of 7 days the mean optical density ($p \leq 0.05$) of the Fe-based HEAs was significantly higher as compared to the control. The mean optical density ($p \leq 0.05$) of the Fe-based HEAs was highest for 7 days as compared to 3 and 5 days with the control. It was observed that in HEA2 and HEA3 there is no the statistically significance differences at $p \leq 0.05$ in the mean optical density (O.D.) for 3, 5, and 7 days. The better biocompatibility of the Fe-based HEAs as compared with 316L is may be due to the presence of Mn, Ti, and Al, which are not present in the 316L. The Mn, Ti, and Al elements improve the biocompatibility in the Fe-Mn based alloys, 316L, and pure Fe, respectively [282, 290, 291] . The severe lattice distortion in the HEAs give unusual properties in HEAs due to the existence of different atoms having different atomic size, and cocktail effect [26, 292]. The enhancement in biocompatibility in the Fe-based HEAs might be due to lattice distortion, as earlier it has been reported that the lattice distortion increased the biocompatibility in Ti and Ti-based alloys [293, 294]. Due to the cocktail effect, as the presence of individual elements and the influence of elemental mixture could have led to such an improvement in the biocompatibility in HEAs [295]. As it was observed in the conventional alloys that the small

addition of Ni increased the biocompatibility [296, 297], as it was also observed in the present Fe-based HEAs.

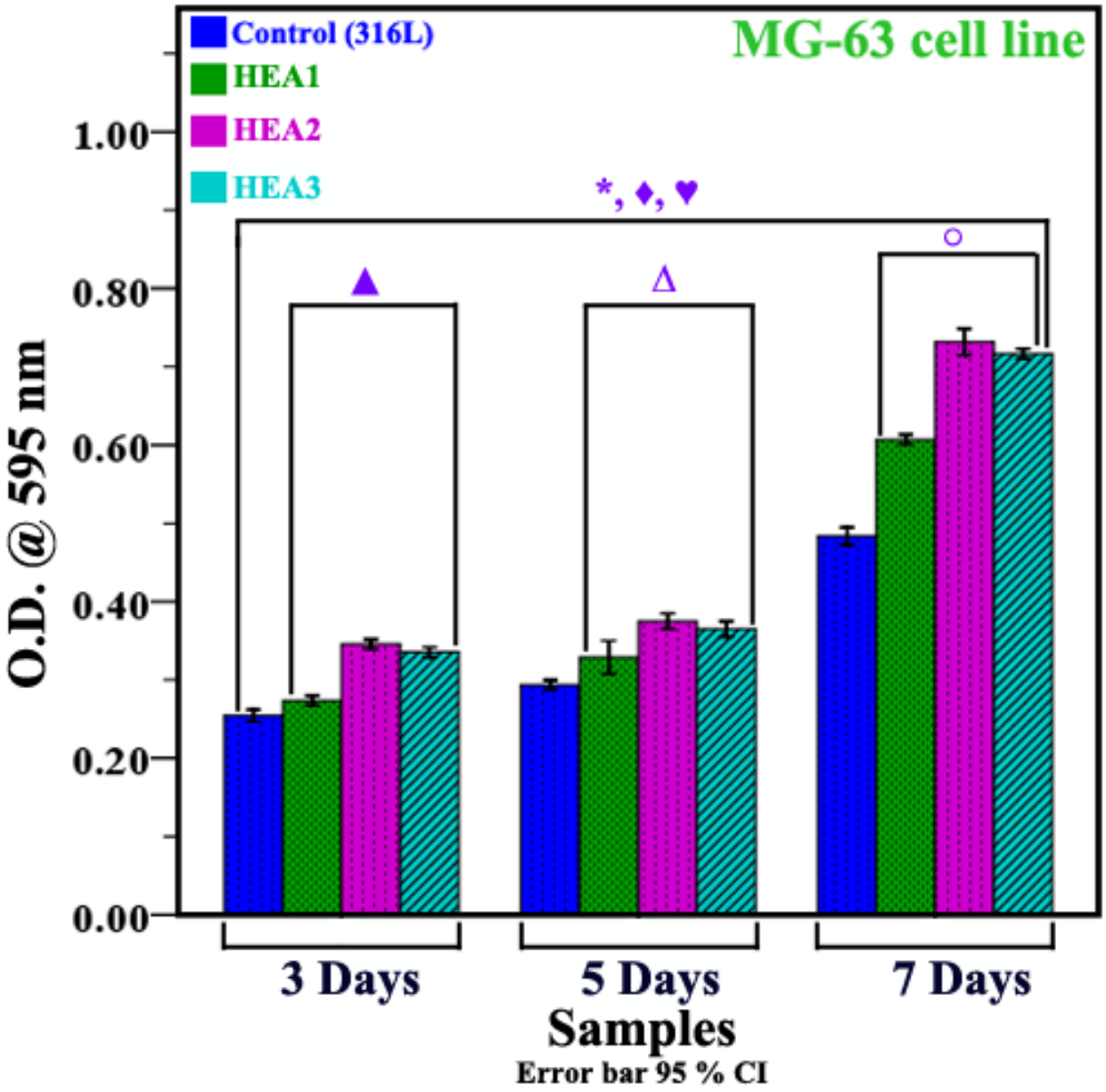

Figure 6.22: Concentration-dependent quantitative analysis (MTT assays) of control (316L) and SPSed samples of HEA1, HEA2, and HEA3 in mesenchymal stem cell (MG-63) after 3, 5, and 7 days. The symbol (*, ♦, ♥) symbolizes the statistically significance differences at $p \leq 0.05$ in the mean optical density (O.D.) among the HEA1, HEA2, and HEA3 with 316L treated for 3, 5, and 7 days, respectively. The statistically significance differences at $p \leq 0.05$ of HEA1 with HEA2 and HEA3 preserved for 3, 5 and 7 days (means (▲, Δ, ●)), respectively.

6.9 Discussion

6.9.1 Alloying behaviour and microstructure

The phase evolution during the milling for the HEA1, HEA2, and HEA3 are as follows: at 0 h, the diffraction peaks of all the elements are present. At 10 h, the higher angle diffraction peaks and the peaks corresponding to Al disappeared. The disappearance of the Al element showed that the Al has the highest alloying rate. At 20 h, Cr and Ni (only in HEA2 and HEA3) disappeared. At 30 h, the Mn and Ti disappeared, and the dual-phase solid solution formed with BCC and χ-type phase structure. There was no phase change occurred up to 40 h. The alloying rate behaviour was discussed in terms of melting point and diffusion coefficient in the $Cu_{0.5}$NiAlCoCrFeTiMo HEA system [298]. The BCC phase formed with α-Fe as the host lattice as concluded from the fact that the BCC phase has lattice parameter similar to that of the α-Fe; the concept of host lattice after the milling was discussed in Vikas et al. [299]. The χ-type phase (close to gamma-brass structure) was also formed after the mechanical milling in the $(Fe_{0.3}Ni_{0.3}Mn_{0.3}Cr_{0.1})_{88}Ti_4Al_8$ HEA [287]. They stated that the χ-type phase formed during mechanical milling is metastable and further transform at elevated temperatures [273]. It was also observed in conventional dual-phase steel (mostly contain Mo) that the χ-type phase is further transformed in to σ phase at above 650 °C [273]. The physical and chemical properties of the constituent elements are given in Table 2.3.

Phase formed after mechanical alloying and spark plasma sintering was associated with the thermodynamic parameters i.e., ΔS_{conf}, ΔH_{mix} and δ, and its calculations are given in equation no. 1.2, 1.3, and 1.6, respectively. The calculated values of the thermodynamic parameter for the Fe-based HEAs are mentioned in Table 6.8. Two more parameters are proposed i.e., valence electron concentration (VEC) and Ω parameter for the prediction of solid solution formation in the HEAs, and it is calculated using equation no. 1.7 and 1.8, respectively. The VEC is used to predict the

FCC/BCC or both phase formation in the HEAs. The VEC is well within the range of BCC phase formation in the case of HEA1 and HEA2, and in the case of HEA3, it is in dual-phase region, and in present alloy systems BCC phase formed after the mechanical alloying. So, the alloy formed the BCC phase structure after the milling but transformed into BCC + FCC at elevated temperatures. So, the formation of the FCC phase at elevated temperatures may be due to the binary enthalpy between the Fe-Mn and Mn-Cr being positive, and its value is mentioned in Table 6.9. The equiatomic AlCrFeMnTi HEA formed the dual-phase structure consisting of BCC and FCC after VAM [300–302]. $(FeNi)_{67}Cr_{15}Mn_{10}Al_{8-x}Ti_x$ (x = 3, 4 and 5 at. %) HEAs prepared using the VAM, and it formed the dual-phase structure of FCC and γ′[139].

The lattice parameters of the BCC and FCC phase decrease as the Ni content increases and Cr content decreases, this is due to the fact that the smaller atomic size element (Ni) is replacing the bigger atomic size element (Cr). This kind of decrease in lattice parameter in the FCC phase is also observed in AlCoCrCuFeNi HEA when the atomic percent of Al decreases and the atomic percent of other elements present in the alloy increases [303].

Table 6.8: Thermodynamic parameter of Fe-based HEAs.

Thermodynamic parameter	**ΔH_{mix} (kJ/mol)**	**ΔS_{conf} (J/K-mol)**	**δ (%)**	**Ω (Dimensionless)**	**VEC (Dimensionless)**
HEA1	-5.7	12.23	6.3	3.7	6.5
HEA2	-5.8	13.16	6.3	3.8	6.7
HEA3	-6.5	13.38	6.3	3.5	6.9

Table 6.9: Binary enthalpies (kJ/mol) of all possible binary combination in HEA1, HEA2, and HEA3.

Binary Alloys	Binary Enthalpy (kJ/mol)		
	HEA_20_00	HEA_15_05	HEA_10_10
Fe-Mn	1	1	1
Fe-Cr	-4	-3	-2
Fe-Ni	---	-3	-6
Fe-Ti	-41	-41	-41
Fe-Al	-36	-36	-36
Mn-Cr	4	4	3
Mn-Ni	---	-10	-16
Mn-Ti	-18	-18	-18
Mn-Al	-37	-37	-37
Cr-Ni	---	-6	-8
Cr-Ti	-11	-11	-11
Cr-Al	-15	-15	-15
Ti-Ni	---	-27	-43
Ti-Al	-43	-43	-43
Ni-Al	---	-19	-30

6.9.2 Thermal stability

The thermal stability of the 40 h milled powder was estimated through DSC analysis from 200 ℃ to 1000 ℃ and it correlated with the ex-situ XRD analysis of the annealed samples at 25 ℃,

400 ℃, and 600 ℃. After 400 ℃, the alloy retained the metastable solid solution (BCC and χ-type phase structure). Afterward at 600 ℃, the FCC solid solution evolve, which was correlated with the exothermic peak in between 500 ℃ - 550 ℃ for the Fe-based HEAs. After sintering, the phase formed mostly containing the BCC and FCC along with χ-type phase as precipitates. In the present alloy systems, the BCC phase was retained after the sintering, this kind of thermal stability of BCC was observed in the previously reported HEAs [181]. The non-equiatomic AlCrFeMnTi HEAs, showed the good thermal stability after annealing treatment at 750 ℃, 850 ℃, and 1200 ℃ for 168 h [150]. The phase transformations in present alloy systems occurred at higher temperatures were due to the formation of metastable solid solution after the milling. Figure 6.23, 6.24, and 6.25(a) illustrates the predicted equilibrium phase fraction as a function of temperature ranging from 50 ℃ to 1450 ℃ of Fe-based HEAs using steel database TCFE8. According to the Thermocalc calculation, the equilibrium phases in HEA1 are three BCC_A2, and in HEA2 and HEA3 are three BCC_A2 and FCC_A1, respectively. BCC_A2 predicted phase is rich in Cr and Fe, and it is stable up to 1400 ℃. At lower temperatures, the BCC_A2#2 phase was predicted which is rich in Cr and Mn, formed around 550 ℃ and stable down to 50 ℃. Figure 6.23(b-e), 6.24(b-f), and 6.25(b-f) shows the amount of phases versus temperature in HEA1, HEA2, and HEA3, respectively, and the elemental composition in all the phases and their stability with respect to temperature for BCC_A2, BCC_A2#2, BCC_A2#3, FCC_A1 and liquid, respectively. The phase formed after the milling, annealed and SPS have some disagreement with the predicted phase from CALPHAD. In HEA1, at elevated temperature, it forms the FCC phase but ThermoCalc predicted three BCC phases, and Cr and Mn rich BCC_A2#3 phase predicted phase at room temperature and stability below 100 ℃. This kind of phase formation is not observed in

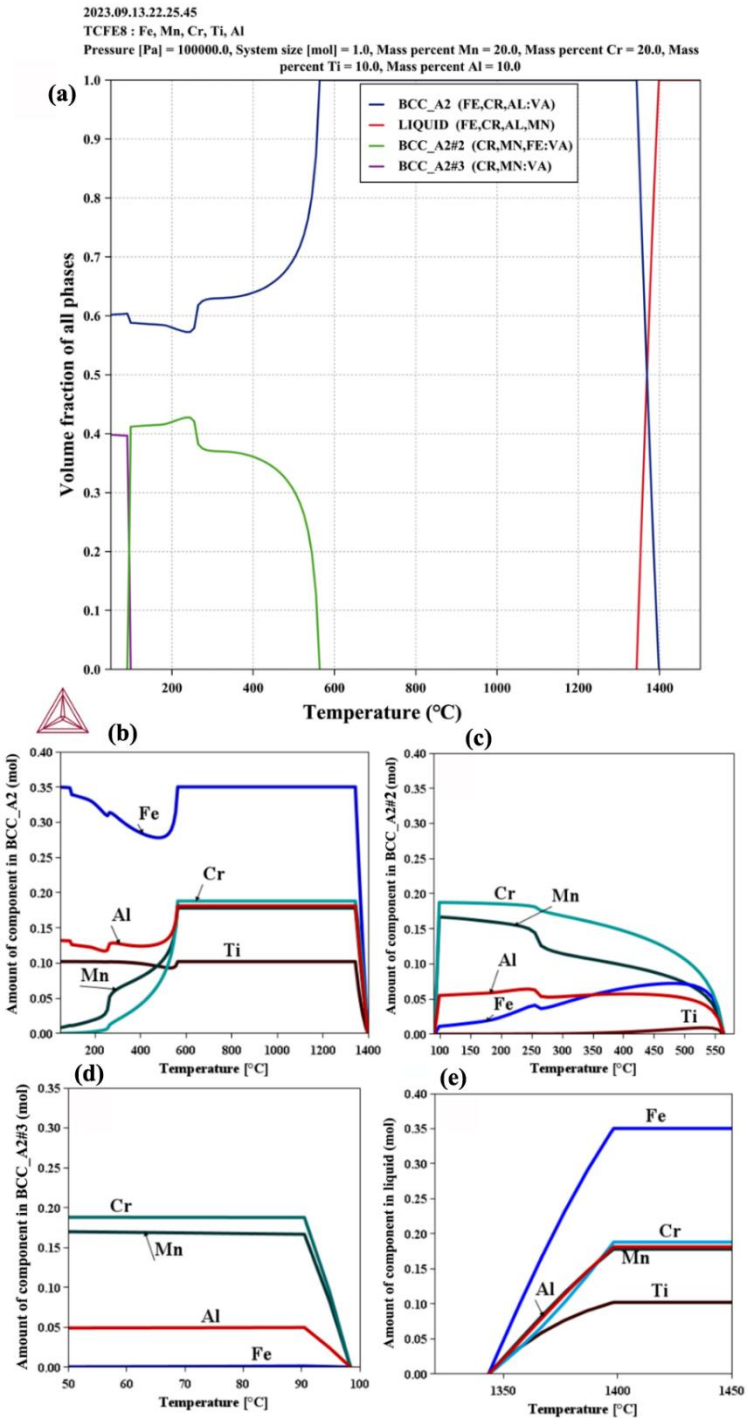

Figure 6.23: (a) Property diagram of HEA1 (TCFE8); (b-e) Amount of component in the BCC_A2, BCC_A2#2, BCC_A2#3, and liquid, respectively where they are stable in the temperature range.

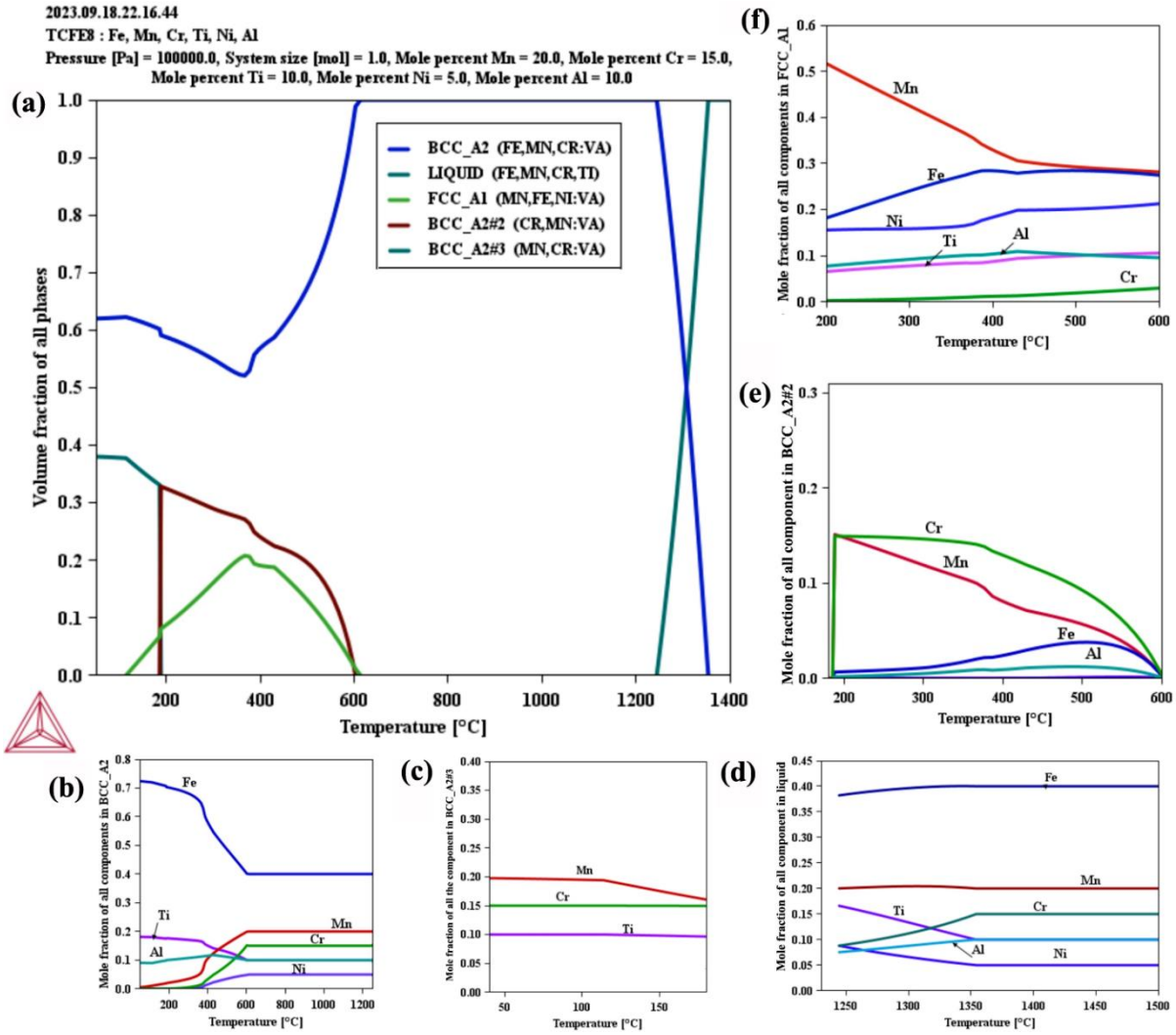

Figure 6.24: (a) Property diagram of HEA2 (TCFE8). (b-f) Amount of component in the BCC_A2, BCC_A2#3, liquid, BCC_A2#2, and FCC_A1, respectively where they are stable in the temperature range.

experimental findings. Similar in HEA2 and HEA3, two types of BCC phase and one FCC phase formed, but CALPHAD predicted BCC_A2#3 phase rich in Cr and Mn predicted room temperature and stability below 100 ℃, and phase fraction of FCC phase is different in experimental finding and predicted phase. This disagreement could be a consequence of the description being limited to the extrapolation of the ThermoCalc database and thus failing to predict phases that would be stable in a multi-component system.

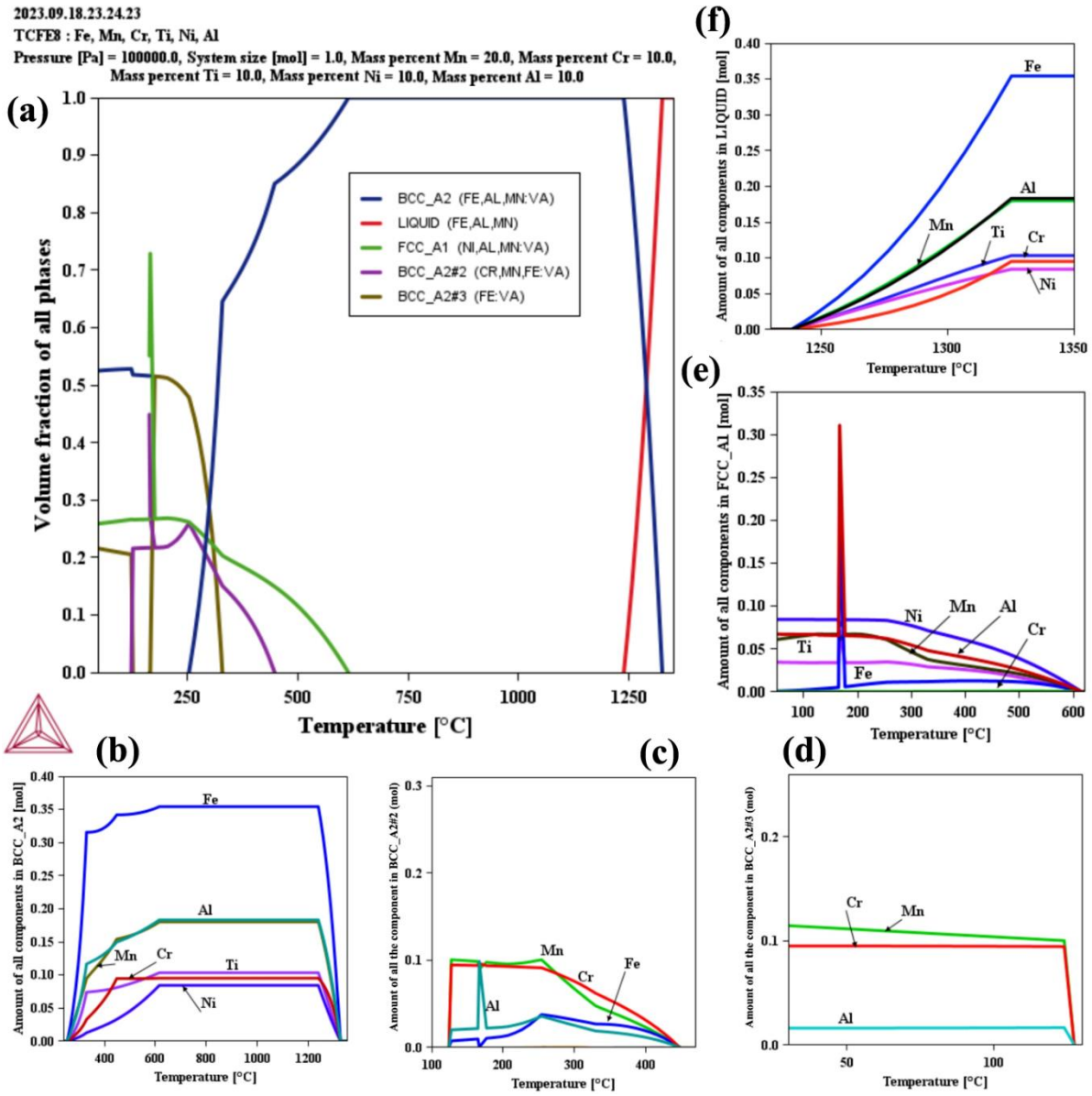

Figure 6.25: (a) Property diagram of HEA3 (TCFE8). (b-f) Amount of component in the BCC_A2, BCC_A2#2, BCC_A2#3, FCC_A1, and liquid, respectively where they are stable in the temperature range.

6.9.3 Mechanical properties and strengthening mechanism

The measured yield stress (σ_{ye}) values of the SPSed samples of the HEA1, HEA2, and HEA3 are found to be 1962, 1810, and 1320 MPa and it is the combination of the various strengthening mechanisms i.e., frictional internal stress, grain-boundary, precipitates, dislocation and solid

solution strengthening, which is given in equation no. 1.9. The frictional stress was taken as 120 MPa and 95.4 MPa for BCC and FCC [225, 285], respectively.

The grain boundary strengthening was calculated using equation no. 1.13, where, K_o is the constant related to the material and the value was taken as 823 MPa/$\mu m^{1/2}$ and 574 MPa/$\mu m^{1/2}$ for FCC and BCC [225, 285], respectively, and d represents the grain size, and its values are 0.84 μm, 1.04 μm, and 2.36 μm for HEA1, HEA2, and HEA3, respectively. The value of grain boundary strengthening for HEA1, HEA2, and HEA3 is found to be 1796 MPa and 630 MPa for FCC and BCC, 806 MPa and 846 MPa for FCC and BCC, 536 MPa and 1015 MP for FCC and BCC, respectively.

The effect of χ-type phase nanoprecipitates in the FCC and BCC phase of the non-equiatomic HEAs, which is calculated from equation no. 1.14 and 1.15. The values of the following term in the formulae are, M = 3.05 and 2.73 for FCC and BCC [225, 285], respectively, G is the shear modulus, calculated using the rule of mixture, and its value is found to be 78.78 GPa, 77 GPa, and 75 GPa for HEA1, HEA2, and HEA3, respectively, υ is 0.3 , b is the Burger vector, f is the volume fraction of the precipitates, which is mentioned in Table 6.5, r = average radius of the precipitates (78 nm, 125 nm, and 115 nm for χ-type phase). The value of the nanoprecipitates of χ-type phase strengthening for the BCC phase is 197 MPa, 146 MPa, and 150 MPa for HEA1, HEA2, and HEA3, respectively. The effect of χ-type phase nanoprecipitates in the FCC phase in term of strengthening values are 197 MPa and 174 MPa for HEA2 and HEA3, respectively.

The contribution of the dislocation strengthening was calculated using equation no. 1.12. The value of α is taken as 0.2 [285], b is the Burger vector and ρ_{dd} is the dislocation density, calculated using the equation 2.1, and the values of crystallite size, micro strain, and lattice parameter are

given in Table 6.5. The values for HEA1, HEA2, and HEA3 was found to be 668 MPa and 418 MPa for BCC and FCC, 491 MPa and 612 MPa for BCC and FCC, 591 MPa and 468 MPa for BCC and FCC, respectively.

The effect of solid solution strengthening is estimated by equation no. 1.10 and 1.11. Al and Ti, and Al and Mn were taken as solute elements for the BCC, and FCC, respectively, and their value are given in Table 6.6. The value for HEA1, HEA2, and HEA3 was found to be 198 MPa and 272 MPa for BCC and FCC, 251 MPa and 195 MPa for BCC and FCC, 204 MPa and 201 MPa for BCC and FCC, respectively.

Figure 6.26(a, b, and c) show the values of the various strengthening mechanism and experimental strength for HEA1, HEA2, and HEA3, respectively. The dominant strengthening mechanisms for the non-equiatomic HEAs is the grain boundary and dislocation. In case of HEA1, the precipitate strengthening is also the dominant mechanism. The contribution (%) of different strengthening mechanisms is shown in Figure 6.26(d, e, and f). The percentage calculations for HEA1, HEA2, and HEA3 are done to take the contributions of BCC and FCC phase are 78.3 % and 21.7 %, 67 % and 33 % for FCC and BCC, 87.7 % and 12.3 % for FCC and BCC, respectively. The calculated theoretical strength and the measured strength of the alloys are somewhat different, this is due to the some of the constant values are considered from references. The ultimate compressive strength in the previously reported non-equiatomic AlCrFeMnTi HEAs is listed in Table 1.3. Liaw et al. [150] discussed the strengthening mechanism in the non-equiatomic AlCrFeMnTi HEAs through the In-situ neutron-diffraction

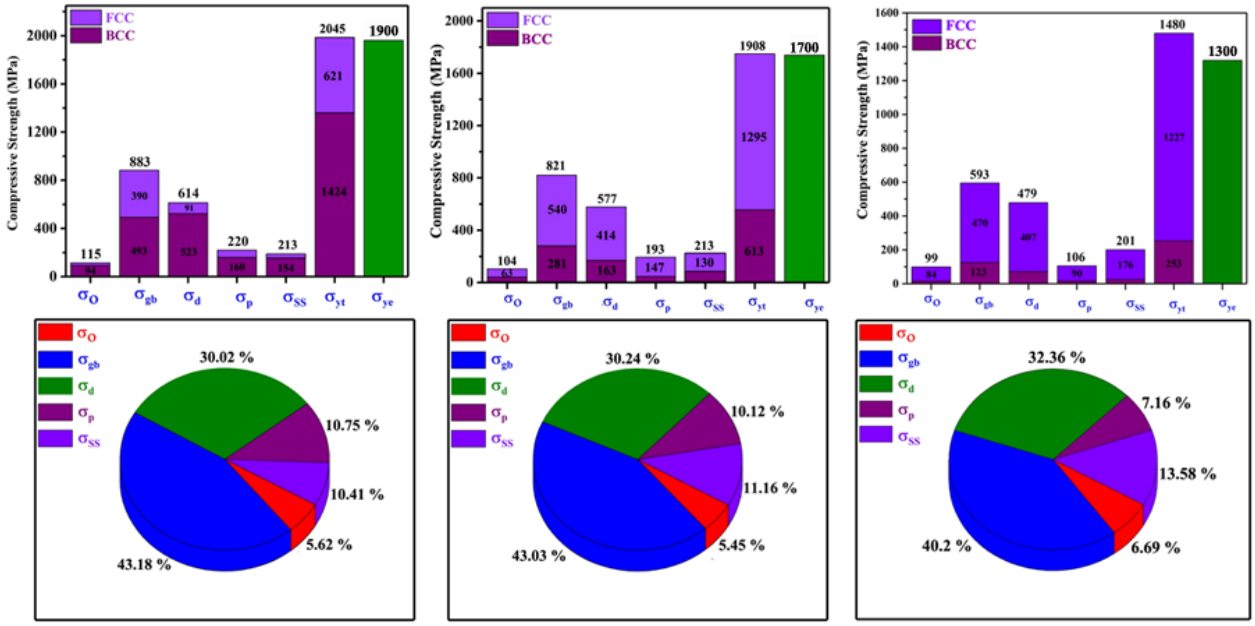

Figure 6.26: (a, b, and c) The values of the various strengthening mechanism and yield strength of the HEA1, HEA2, and HEA3, respectively (Bar plot); (d, e, and f) The pie chart for the percentage's contribution of the various strengthening mechanism of the HEA1, HEA2, and HEA3, respectively.

experimental during the uniaxial compressive load in the $Al_{20}Cr_5Fe_{50}Mn_{20}Ti_5$ (Fe-HEA1) and $Al_{30}Cr_5Fe_{50}Mn_{10}Ti_5$ (Fe-HEA2), which showed that the precipitation strengthening and intrinsic-deformation mechanism were the dominant mechanism. But the precipitation strengthening was more dominant in Fe-HEA1, and in Fe-HEA2 the intrinsic-deformation mechanism was dominant. The superior mechanical properties in $(FeNi)_{67}Cr_{15}Mn_{10}Al_{8-x}Ti_x$ (x = 3, 4 and 5 at. %) HEAs are due to the strain-hardening behaviours and deformation micro-mechanisms strengthening mechanism [139]. The $Fe_4Ni_4Mn_2CrTi$ HEA showed good mechanical properties due to the solid-solution, grain-boundary, and precipitation strengthening mechanism [304]. Precipitates strengthened $(Fe_{0.3}Ni_{0.3}Mn_{0.3}Cr_{0.1})_{88}Ti_4Al_8$ HEA showed the 2151 MPa ultimate compressive strength [287]. The present alloys showed good ultimate compressive strength as compared with almost all the HEAs listed in Table 1.3. The present alloy showed excellent compressive strength

with an appreciable amount of ductility as compared with low-density steel and conventional dual-phase ferritic steel. The elastic constant decreases as the Ni content increases in the present alloy system; similar kind of behaviour was also observed in $Fe_{20}Mn_{20}Co_xCr_yNi_{(60-x-y)}$ ($0 \leq x \leq 30$, $0 \leq y \leq 35$) HEAs [303]. The elastic constant first increases and then decreases as the Cr content increases and Ni content decreases, suggesting that the resistance to deformation changes accordingly at the elastic stage.

6.10 Conclusion

The structural, microstructural formation, and thermal stability of $Fe_{40}Mn_{20}Cr_{20-x}Ni_xTi_{10}Al_{10}$ HEAs after milling and spark plasma sintering were evaluated. The mechanical properties i.e., microhardness, elastic modulus, and compressive strength of the SPSed sample were also evaluated. Further, the wear and biocompatibility of the SPSed sample were also carried out systematically. The following conclusions were drawn from the present chapter;

1. The BCC and χ-type phase structure (close to gamma-brass structure) formed after 40 h of mechanical milling. The present alloy systems demonstrated the thermal stability up to 400 ℃, and afterward formed the FCC solid solution in between 500 ℃- 600 ℃.
2. The BCC phase was retained and the FCC phase was evolved after the sintering (SPS) at 900 ℃ and 50 MPa. As the Ni content increases from x= 0 to 10 at. %, the fraction of the FCC phase increases.
3. The microhardness, elastic modulus, yield compressive strength, and strain of the SPSed sample decreased from 6.4 GPa to 4.2 GPa, 183 to 127 GPa, 1962 MPa to 1320 MPa and 6.7 to 15.8 %, as the Ni content increases from x = 0 to 10 at. %, respectively.

4. The wear properties of HEA1, HEA2, and HEA3, were done systematically by varying the load condition and it was found that the specific wear rate was increased as the phase transformation from BCC major phase to FCC major phase and by increasing load.
5. In-vitro biocompatibility of the SPSed samples of the Fe-based HEAs was done under Osteosarcoma MG-63 cell for 3, 5, and 7 days, and it showed better cell proliferation with 316L. Overall the HEA2 showed the better biocompatibility among the three Fe-based HEAs. This alloy also has good combination of strength and ductility, lower elastic modulus value, good wear resistance, and better biocompatibility as compared with 316L, and therefore this alloy system can be a potential biomaterial for implant applications.
6. The calculated values of strengthening were close to the experimental values. The grain boundary and dislocation strengthening were dominant mechanisms in all the present alloy systems. The phase prediction through thermodynamic parameters was well correlated with the experimental results after the mechanical milling, annealed sample, and SPS.